The lateral boundary of a metamorphic core complex: The Moutsounas shear zone on Naxos, Cyclades, Greece

Shuyun Cao [a,*], Franz Neubauer [a], Manfred Bernroider [a], Junlai Liu [b]

[a] Dept. Geography and Geology, University of Salzburg, Hellbrunnerstr. 34, A-5020 Salzburg, Austria
[b] State Key Laboratory of Geological Processes and Mineral Resources, China University of Geosciences, Xueyuan Rd. 29, Haidian, Beijing 100083, China

ARTICLE INFO

ABSTRACT

We describe the structure, microstructures, texture and paleopiezometry of quartz-rich phyllites and marbles along N-trending Moutsounas shear zone at the eastern margin of the Naxos metamorphic core complex (MCC). Fabrics consistently indicate a top-to-the-NNE non-coaxial shear and formed during the main stage of updoming and exhumation between ca. 14 and 11 Ma of the Naxos MCC. The main stage of exhumation postdates the deposition of overlying Miocene sedimentary successions and predates the overlying Upper Miocene/Pliocene conglomerates. Detailed microstructural and textural analysis reveals that the movement along the Moutsounas shear zone is associated with a retrograde greenschist to subgreenschist facies overprint of the early higher-temperature rocks. Paleopiezometry on recrystallized quartz and calcite yields differential stresses of 20–77 MPa and a strain rate of 10^{-15}–10^{-13} s^{-1} at 350 °C for quartz and ca. 300 °C for calcite. Chlorite geothermometry of the shear zone yields two temperature regimes, 300–360 °C, and 200–250 °C. The lower temperature group is interpreted to result from late-stage hydrothermal overprint.

1. Introduction

Structural evolution of metamorphic core complexes (MCCs) is critical to understanding large-scale extension is accommodated exhumation of mid- to lower-crustal levels. A gneissic core is often overlain by a low-angle extensional detachment, that juxtaposes lower metamorphic grade to supracrustal rocks (e.g., Davis, 1983; Coney and Harms, 1984; Coney, 1987; Wernicke, 1985, 1988; Lister and Snoke, 1984, 1989; Whitney et al., 2013). The development of an MCC is relative to the progression of different metamorphic stages during exhumation, producing a characteristic sequence of (overprinted) meso- and microstructures and textures within the low-angle extensional detachment along upper margins of the MCC. Structural observations, kinematic criteria, microstructural fabrics and metamorphic histories need to be examined in great detail within low-angle normal shear zones, as these features are often the key to constrain critical aspects of metamorphic core complex formation. Quantitative studies of microstructures and textures in MCCs often present important inferences on, e.g., deformation processes, deformation temperatures, strain state and deformation mechanisms and rheology that operated in exhumed shear zones on top of the MCC (e.g. Toy et al., 2008; Whitney et al., 2013). Mylonitic rocks within a ductile shear zone are commonly characterized by a steady-state microfabric, e.g., with a stable grain size distribution, shape-preferred orientation and crystallographic preferred orientation (CPO). The balance between individual strain-accommodating processes, texture development and different deformation mechanisms are related to succession of physical conditions of deformation, e.g., temperature, strain rate, grain size, fluid activity (e.g. Hirth and Tullis, 1992; Rutter, 1998; Liu et al., 2002; Stipp et al., 2002; Schenk et al., 2005) and second-phase particles (e.g. Herwegh and Kunze, 2002). The temperature is decreasing and the differential stresses and fluid flow typically increase within detachment zones during exhumation. It is also widely believed that a general rheological weakening associated with grain-size reduction by dynamic recrystallization occurs (e.g. de Bresser et al., 2001 and references therein). Asymmetric fabrics and textures relative to the meso-structural framework (e.g., foliation and lineation) may yield a criterion for the strain history and sense of shear (e.g. Wenk et al., 1987; Bestmann et al., 2000).

MCCs typically occur within the south-central Aegean area (e.g. Lister et al., 1984; Urai et al., 1990; Wawrzenitz and Krohe, 1998; Brun and Sokoutis, 2007; Jolivet et al., 2010; Grasemann

* Corresponding author.
 E-mail addresses: shuyun.cao@sbg.ac.at, shuyuncao@163.com (S. Cao).

et al., 2012). A classic metamorphic core complex is located on the island of Naxos in the Aegean Sea and numerous high-quality structural and microfabrics data have been published (e.g. Urai et al., 1990; Buick, 1991a,b; Gautier et al., 1993; John and Howard, 1995; Vanderhaeghe et al., 2007; Lewis et al., 1998; Keay et al., 2001; Urai and Feenstra, 2001; Krabbendam et al., 2003; Schenk et al., 2007; Vanderhaeghe, 2004; Vanderhaeghe et al., 2007; Seward et al., 2009; Kruckenberg et al., 2010, 2011). The Naxos-Paros ductile low-angle fault (e.g. Gautier et al., 1993), located along the northern margin of Naxos, is part of the North Cycladic Detachment System (Jolivet et al., 2010) (Figs. 1 and 2). A rolling hinge top-N displacement was proposed in recent models (Jolivet et al., 2009). Exhumation of the Naxos MCC was contemporaneous with migmatization and granitoid intrusion in the center of

the dome. The Naxos migmatite contains subdomes, which formed by combination of upper crustal extension and deep crust contraction (Kruckenberg et al., 2010., 2011), The vast majority of the deformation in the migmatitic core is characterized by melt-present deformation conditions and microstructures show recrystallization at high-temperature. Melt-present deformation clearly was the key deformation process in the core of the dome throughout its history (e.g. Vanderhaeghe, 2004; Kruckenberg et al., 2010, 2011; Siebenaller et al., 2013).

Detailed information of the eastern boundary shear zone of the Naxos MCC is poorly known (e.g. Vanderhaeghe et al., 2007). The aim of this paper is to describe this low-angle ductile shear zone on the eastern boundary of the Naxos MCC and we denote this fault as the Moutsounas shear zone. Field structures combined with
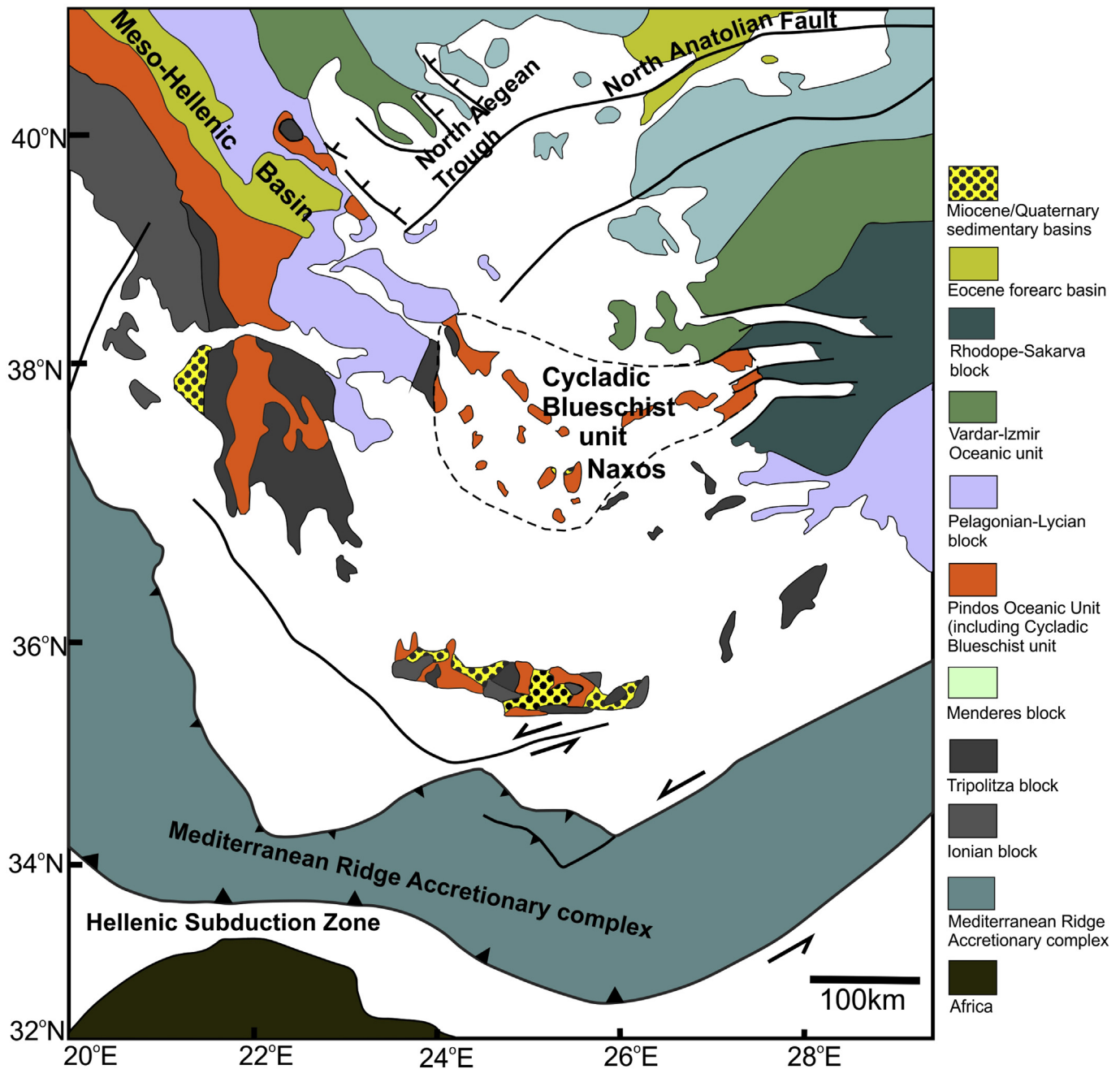

Fig. 1. Simplified tectonic map of the Aegean region showing the main tectonic zones above the Hellenic subduction zone (modified after Jolivet et al., 2010; Ring et al., 2010).
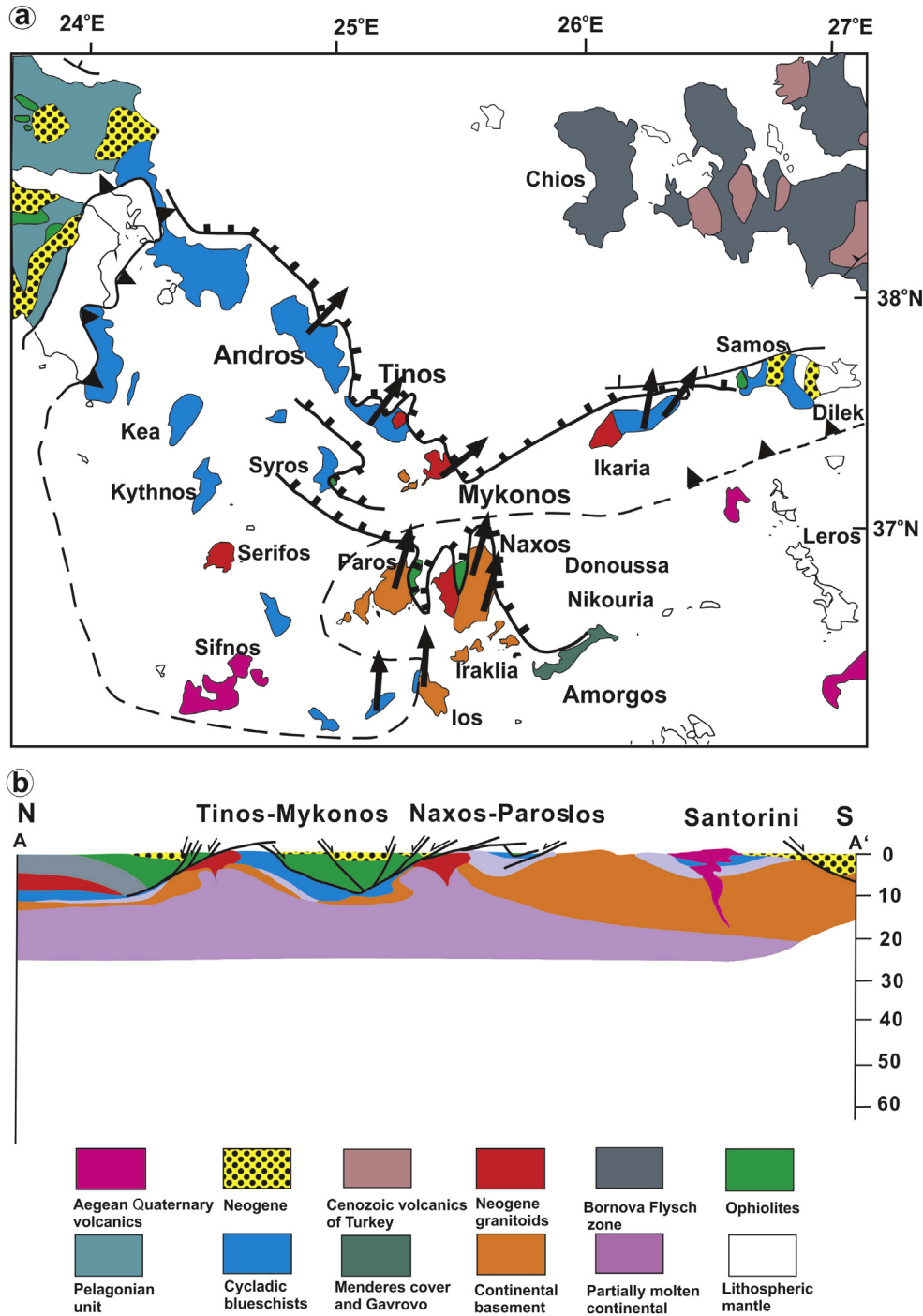
Fig. 2. (a) Schematic geological map within the context of the North Cycladic Detachment System. The arrows indicate the sense of ductile shear in the lower plate (modified after Jolivet et al., 2010; Huet et al., 2011). (b) Detail of N–S cross-section of the Aegean region centered on the Cyclades archipelago (modified after Jolivet et al., 2010).

microstructural and textural analyses reveal the structural and microfabric evolution in terms of Naxos MCC exhumation, heating from an associated migmatite dome in the footwall and sedimentation on the upper plate. We also present preliminary paleo-piezometric calculations and constraints of the temperature of deformation using chlorite thermometry and phengite barometry. These results, when combined with previous studies, provide new insight into the structural history of the Naxos MCC and into the mode and history of tectonic extension in the Aegean region during Neogene times.

2. Regional geological setting

The southern Aegean Sea is part of the Hellenic subduction system (Le Pichon and Angelier, 1979; Angelier et al., 1982; McClusky et al., 2000; Pe-Piper, 2000; Wortel and Spakman, 2000) (Fig. 1). Earthquake focal mechanisms (e.g., Hatzfeld et al., 1993; Bohnhoff et al., 2004; Hollenstein et al., 2008; Floyd et al., 2010) indicate retreat of the subduction zone to the SW, and associated extension in the Aegean region (Ring et al., 2010 and references therein). Pliocene to present-day arc-related volcanism

developed to the south of the Attic Cycladic massif (Buick, 1991a). The Attic-Cycladic massif and its NW extension in the Pelagonian massif represent the submerged part of tectonic units striking NW–SE in mainland Greece, which turns to ca. E–W strike in the Cyclades. Miocene N–S extension in the Aegean Sea resulted in the sequential north to south formation of numerous MCCs in the Cyclades archipelago (Lister et al., 1984; Lee and Lister, 1992; Boronkay and Doutsos, 1994; Doutsos and Kokkalas, 2001) along the North Cycladic, South and West Cycladic Detachments (Jolivet et al., 2010; Grasemann et al., 2012). During Miocene extension, medium- to high-grade metamorphic rocks were deformed in a W–E to NW–SE compressive and NNE–SSW extensional ductile regime (Lister et al., 1984; Buick, 1991a, b; Walcott and White, 1998). Extension in the region resulted in crustal thinning, tectonic unroofing, and emplacement of melts within the core complex (e.g., Kruckenberg et al., 2011). Tectonic unroofing continued in places until latest Miocene times, as recorded by apatite fission-track cooling ages (Hejl et al., 2002; Brichau et al., 2010). Late Oligocene to Early Miocene crustal thinning was likely facilitated by the collapse of Eocene over-thickened crust and aided by backarc extension related to subduction zone retreat, similar to the recent geodynamic setting (Lee and Lister, 1992; Jolivet and Patriat, 1999; Jolivet et al., 2010).

The Alpine metamorphic history of metamorphic units of this region includes Meso-Hellenic high-pressure metamorphism (M1) at ca. 45 Ma and Neo-Hellenic Barrovian-type metamorphism (M2) between 23 and 16 Ma (Altherr et al., 1982; Andriessen et al., 1987; Wijbrans and McDougall, 1988; Okrusch and Bröcker, 1990; Avigad and Garfunkel, 1991; Avigad, 1998). On the Greek mainland, the Alpine-metamorphic basement domain is juxtaposed against the external arcuate belt of unmetamorphic continental units (Sub-Pelagonian and Ionian units) and the Pindos ophiolite (Jacobshagen, 1986, Fig. 1).

3. Geology of Naxos

Naxos is the largest island of the Cyclades in the western Aegean Sea (Fig. 2a). The exhumation/uplift resulted in a north-south trending elongated dome (Lister et al., 1984; Jolivet et al., 2004, 2010; Ring et al., 2010) (Fig. 3a). The main structure of the Naxos MCC is a migmatite-cored gneiss dome that is structurally overlain by a ductile low-angle normal fault in the east and a steep strike-slip-type fault zone in the west, the latter located in an N–S trending topographic depression. Within the MCC, continental basement, probably of Variscan age (Altherr et al., 1982; Strumpf, 1997; Reischmann, 1998), is capped by a high-grade metamorphic cover succession of Mesozoic carbonates, fine-grained siliciclastic and tuffaceous rocks (Jansen, 1977; Jacobshagen, 1986). The main rock types on Naxos are intercalated marbles and schists that became dismembered within the migmatitic central part (Fig. 3a; Jansen, 1973; Jansen and Schuiling, 1976; Kruckenberg et al., 2011). The western part of Naxos exposes the Miocene Naxos granodiorite. The hanging wall unit of the MCC comprises remnants of unmetamorphic Mesozoic ophiolites and overlying Miocene and Pliocene sedimentary rocks.

The I-type Naxos granodiorite batholith, now in tectonic contact with the Miocene clastic succession, was emplaced ca. 12–14 Ma ago according to U/Pb dating of zircons (e.g. Henjes-Kunst et al., 1988; Pe-Piper et al., 1997; Keay et al., 2001). Rapid cooling of the batholiths is indicated by ca. 12.5 Ma ^{40}Ar/^{39}Ar ages from various minerals (Wijbrans and McDougall, 1988) and ca. 10 Ma K–Ar biotite cooling ages (Pe-Piper et al., 1997). Apatite fission track ages indicate that cooling to ca. 110 °C occurred at 8.2 Ma (Altherr et al., 1982), which was coeval with ongoing top-to-the-north low-angle normal faulting. Ultramylonite, pseudotachylyte and cataclasite

formation close to the northern and western parts of the detachment fault record tectonic activity lasting until nearly surficial conditions were reached (John and Howard, 1995). Pseudotachylyte formation, which is locally intense in the Naxos granodiorite and along the tectonic contact below the ophiolite nappe, is estimated to have occurred at ca. 10 Ma (Andriessen et al., 1979). The reported ages constrain the final juxtaposition of the ophiolite nappe and the Miocene neo-autochthonous cover sequence, which apparently shows no thermal overprint (Kuhlemann et al., 2004; Seward et al., 2009).

Two main successive Alpine metamorphic events affected the metamorphic zoning of the middle and lower units within the Naxos MCC (e.g. Andriessen et al., 1979; Urai et al., 1990; Keay et al., 2001). The earlier high-pressure (HP) − low-temperature (LT) Eocene metamorphism (M1) phase is recorded by relics of blueschist facies minerals preserved in metamorphic rocks of southern sectors of the island (Wijbrans and McDougall, 1986; Avigad, 1998; Avigad and Garfunkel, 1991). ^{40}Ar/^{39}Ar white mica ages of ca. 45 ± 5 Ma document an Eocene age for blueschist metamorphism (Andriessen et al., 1979; Wijbrans and McDougall, 1986, 1988). In the higher grade metamorphic rocks of Naxos, no relics of an HP−LT metamorphism have been identified. Metamorphic rims of zircons yield U−Pb ages ranging from 57 to 41 Ma and are interpreted to reflect fluid-assisted zircon growth during blueschist metamorphism M1 (Martin et al., 2006, 2008). The blueschist metamorphic phase (M1) was later overprinted by a widespread Barrovian type (MP−MT) metamorphism (M2) during the Miocene grading from greenschist facies to amphibolite facies conditions, and reaching partial melting conditions at the deepest structural levels, as attested by the abundant migmatization in the dome core (670 °C, 5–7 kbar) (Jansen and Schuiling, 1976; Buick and Holland, 1989; Wijbrans and McDougall, 1988; Avigad and Garfunkel, 1991; Duchêne et al., 2006; Martin et al., 2006, 2008). Based on ^{40}Ar/^{39}Ar mineral ages, the timing of peak Barrovian-type M2 metamorphism was first estimated to have occurred between 20 and 15 Ma (Wijbrans and McDougall, 1988) and is consistent with new Rb/Sr ages for micas and garnets (Duchêne et al., 2006). External overgrowth rims of the zircons in the core migmatites have ages ranging from 19 to 14 Ma (Keay, 1998; Keay et al., 2001; Martin et al., 2006). Finally, Martin et al. (2006, 2008) found U−Pb zircon ages of ca. 16 Ma for the Barrovian type metamorphism. In the structurally higher metamorphic rocks, the age of MP−MT metamorphism M2 is constrained to between 27 and 19.9 Ma by ^{40}Ar/^{39}Ar phengite dating (Wijbrans and McDougall, 1988).

Previously buried lower crustal rocks were brought into contact with upper crustal units (hanging wall) along the gently N-dipping Naxos/Paros shear zone (Gautier et al., 1993), which is the ductile expression of the Naxos/Paros extensional fault system (Brichau et al., 2006). It has been convincingly argued that high-temperature metamorphism on Naxos developed as consequence of ductile extensional shearing (e.g. Buick, 1991a, b; Gautier et al., 1993). Structural evidence indicates that the hanging wall of the core complex experienced large-scale top-to-the-north (ca. 010°) transport along a low-angle detachment fault (Gautier et al., 1990, 1993; Walcott and White, 1998) with evidence of deformation under ductile conditions (Urai et al., 1990; Buick, 1991b; Gautier et al., 1993) and subsequent brittle (Angelier et al., 1978; John and Howard, 1995) deformation conditions. Extensional deformation started at or before the peak of high-temperature metamorphism, which has been dated at about 20–16 Ma on Naxos (Keay et al., 2001). Zircons from four granite intrusions clearly post-dating metamorphism were also dated by Keay et al. (2001) and range in age from 15.4 to 11.3 Ma, with the main period of magmatic activity at ca. 12 Ma. All zircon and apatite fission track ages on Naxos range between 11.8 ± 0.8 to 9.7 ± 0.8 Ma and 11.2 ± 1.6 to
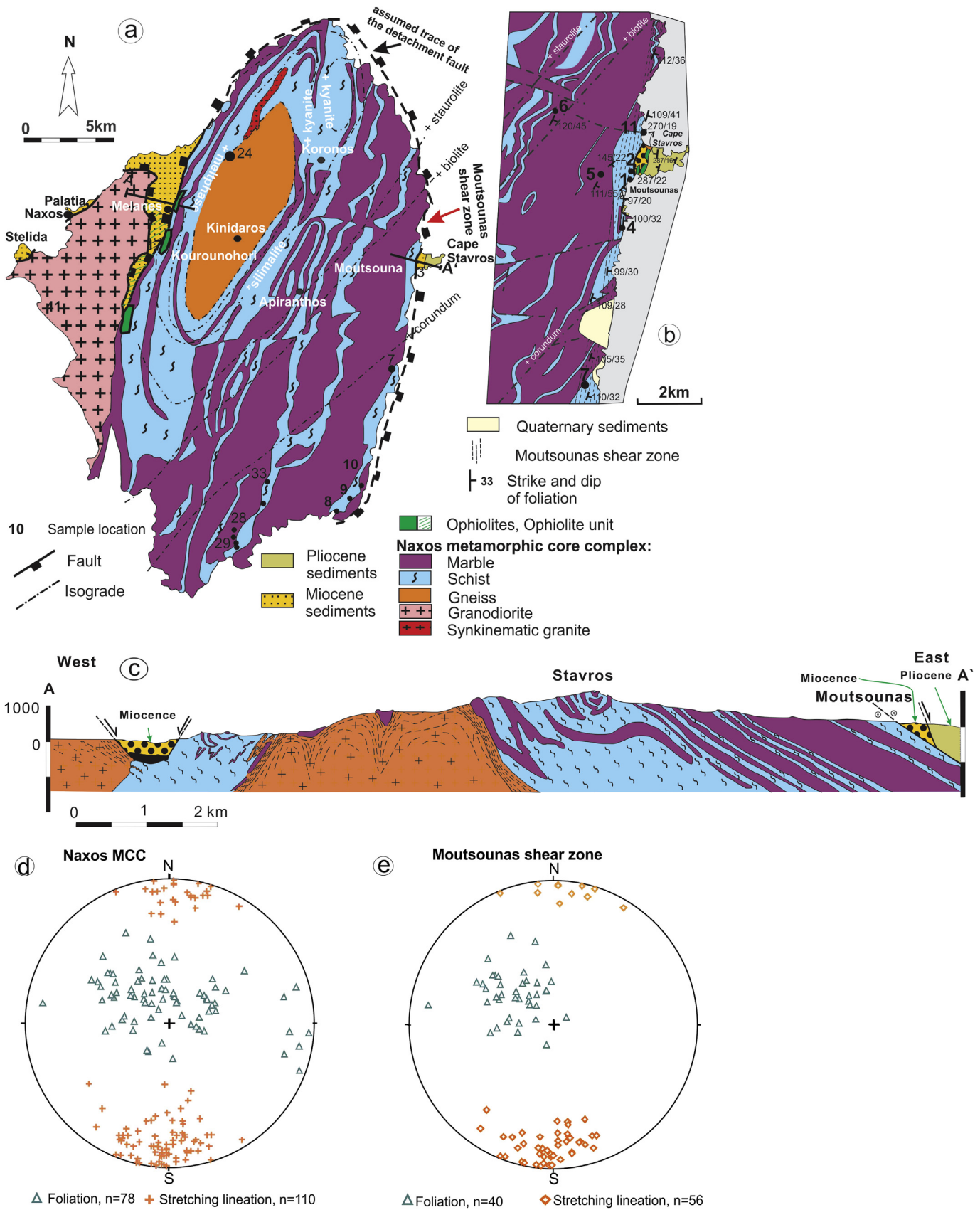
Fig. 3. (a) Geological map of the Naxos MCC in the Cyclades Islands, Greece showing lithologies, metamorphic isogrades and faults with arrows for kinematics after John and Howard, 1995; Keay et al., 2001; Koukouvelas and Kokkalas 2003. (b) Detail of the eastern sectors of Naxos island with sample locations (modified after Jansen, 1977). (c) E–W cross section modified after Vanderhaeghe (2004) and Kruckenberg et al. (2010). Arrows indicate sense of shear retrieved from kinematic analysis of the ductile fabric. (d) Lower hemisphere, eual area stereoplot of foliation planes and stretching lineation (Naxos Island). (e) Stereoplot of foliation planes and stretching lineation (Moutsounas shear zone).

8.2 ± 1.2 Ma and consistently decrease northwards in the direction of hanging wall transport (Hejl et al., 2002; Brichau et al., 2006; Seward et al., 2009). Brichau et al. (2006) interpreted their results to support the scenario of an identical fault dip and a constant or slightly accelerating slip rate of ∼6—8 km per Myr on the Naxos/Paros extensional fault system across the brittle/ductile transition, which separates the MCC from the overlying unit, during exhumation.

Only limited remnants of the hanging wall unit are exposed on the island of Naxos along the western and eastern margins of the Naxos MCC (Fig. 3a; see Jansen, 1977). Hanging wall units comprise an unmetamorphosed strongly disrupted ophiolite nappe (Jansen, 1977) and overlying Miocene and Pliocene sedimentary rocks. The ophiolitic members are serpentinite and basalt, with radiolarite in two spot-like outcrops. Overlying the ophiolite unit, Miocene and Pliocene sedimentary successions are a part of the hanging wall unit, which are exposed on several islands of the Cyclades (e.g., Gautier et al., 1993; Jolivet and Patriat, 1999). Kuhlemann et al. (2004) considered the Miocene clastic succession as the neo-autochthonous cover of the imbricated ophiolite deposited after nappe formation, since both are unmetamorphosed and spatially associated. The Miocene deposits contain no components from the MCC of Naxos, which contrasts coarse-grained Pliocene deposits (Rösler, 1978). Therefore, the Miocene succession is considered to have been deposited prior to exhumation and uplift of the metamorphic complex. This is consistent with cooling ages of the presently exposed footwall rocks (Pe-Piper et al., 1997).

Based on fossil findings, Böger (1983) redefined Neogene formations of Naxos and two formations were distinguished, the Pesulia (23.5—15 Ma) and Eromonisia (11—7.0 Ma) Formations. The Pesulia Fm. comprises marine deposits and turbidites, containing Aquitanian to Early Burdigalian faunas (Angelier et al., 1978; ca. 23—19 Ma), which are well exposed in the center of the island in a fault-bounded block between the metamorphic core and the granodiorite, and in the Cape Stavros peninsula. By means of fission-track dating (30—500 Ma) of detrital zircons, Kuhlemann et al. (2004) report that the sediments were shed from an uplifting mountain region to the south of Naxos and found no high-grade metamorphic pebbles from the Naxos MCC. Seward et al. (2009) concluded from the lack of zircon fission-track ages younger than the stratigraphic age of the center of the island that this formation has not been exposed to temperatures greater than 170—200 °C (the lower bound of the zircon fission-track partial annealing zone) since its time of deposition. Apatite fission track ages from sandstones exposed on Cape Stavros peninsula are 19.8 ± 5.0 18.0 ± 9.6 Ma. From this region, Bargnesi et al. (2012) report (U—Th)/He zircon ages ranging from 270.0 ± 21.6 to 20.7 ± 1.7 Ma indicating a depositional age younger than 20.7 Ma.

Hejl et al. (2003) suggested that paleo-relief features at elevations of 650, 500 and 300—400 m have a maximum age of 8 Ma. Riedl (1982a, b) proposed an Early Miocene to Early Pliocene age for these paleo-erosional surfaces based on climatic and geomorphologic reasoning, which suggests that there has been limited erosion since that period.

4. Moutsounas shear zone

The Mountains shear zone is an N-trending and E-dipping ductile to semi-ductile shear zone along the eastern boundary of the Naxos MCC (Figs. 3 and 4). The shear zone is variably thick, ca. 100—200 m in structural thickness, and similar fabrics can be traced from north of Moutsounas along coastal exposures to the southeastern edge of Naxos.

In the field, the shear zone can be recognized by high-strain zones, fine grain sizes of rock forming minerals, and chloritization, which increases toward the top. Exposures are located between the biotite-in and corundum-in isogrades of the Barrovian type M2 metamorphism proposed by Jansen and Schuiling (1976) representing the chlorite-sericite zone, for which Andriessen et al. (1979) propose a temperature of 420—500 °C. The Moutsounas shear zone is located in the center of this zone and may

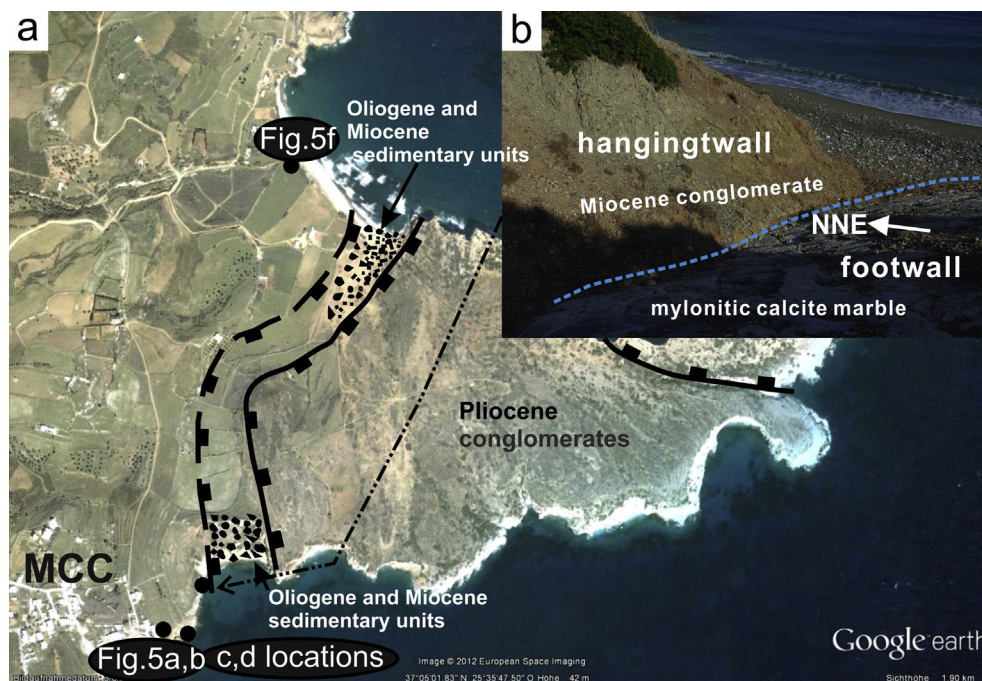**Fig. 4.** (a) Satellite image (Google Earth) of Moutsounas peninsula. View onto cape Stavros peninsula and geological structures. Islands in the background expose marble from the MCC and Oligocene-Pliocene sedimentary succession to the eastern margin. (b) Field coutcrop MCC/Moutsounas at location A. Upper boundary of the MCC with mylonitic calcite marble in the footwall and brittle-deformed Miocene conglomerate in the hangingwall.

represent, therefore, as a rough metamorphic temperature estimate, ca. 420–450 °C in terms of the M2 metamorphism. The southern edge of the Moutsounas shear zone is close to the location, for which Avigad (1998) found ca. 470 °C and 12 kbar for the M1 metamorphism.

The widespread development of mylonitic rocks derived from micaschist, marble and phyllite constitute the main part of the Moutsounas shear zones in the Naxos MCC (e.g. Figs. 4 and 5). Mylonitic quartzite and calc-schists are exceptionally well-developed and occur as discrete layers and lenses within the mylonitic micaschists and phyllites. Thin marble layers are prominent rock types along the Moutsounas shear zone. Marbles grade from basal coarse-grained mylonitic varieties into ultramylonites at the top of the shear zone. On an outcrop scale, S-L fabrics with the development of a mylonitic foliation and a pronounced NNW- to NNE-trending stretching lineation in the calcite-quartz-schist or micaschists are typical indicators of deformation (Fig. 5a and b). The orientations of stretching lineation and foliation (Fig. 3d) are similar to such reported in previous studies, e.g. Urai et al. (1990). Foliation is defined primarily by the preferred orientation of planar minerals (e.g. parallel alignment of mica, chlorite) and by flattened and elongated quartz ribbons, feldspar, chlorite and white mica grains or porphyroclasts. The lineation is defined by the preferred alignment of asymmetric feldspar porphyroclasts, quartz rods, stringers of quartz grains, elongated aggregates of recrystallized feldspars and smeared-out mica flakes. The foliation strikes NNE–SSW or N–S and dips moderately to the E or ESE at a low-angle in the schist, quartzite, marble and phyllite (Fig. 5d). These rocks show evidence of annealing during later heating and grade into retrogressed sheared rocks toward the Moutsounas Peninsula. Mineral stretching lineation in micaschists and phyllites plunges gently (<30°) to NNE or SSW.

The widespread occurrence of asymmetric fabrics, e.g. sheared veins, shear bands, sigmoid fabrics, sigma- and delta-porphyroclasts, asymmetric fringes around rigid clasts and oblique mineralized extensional veins, consistently indicate top-to-the-NNE shear. S–C fabrics are formed with S-planes defined by grain aggregates of elongated quartz and fractured plagioclase and C-planes by chlorite and biotite grains (Fig. 5a and c). In some cases, symmetrically strained mesoscopic structures such as pressure shadows around rigid objects and boudinage of quartz rods are observed. Additionally, late-stage, semi-ductile deformation is locally developed within the shear zone, generally with ~E–W trending steeply N-dipping quartz-filled extensional veins (Fig. 5d).

The shear zone is structurally overlain by hydrothermally altered Miocene conglomerates, which contain no pebbles from the
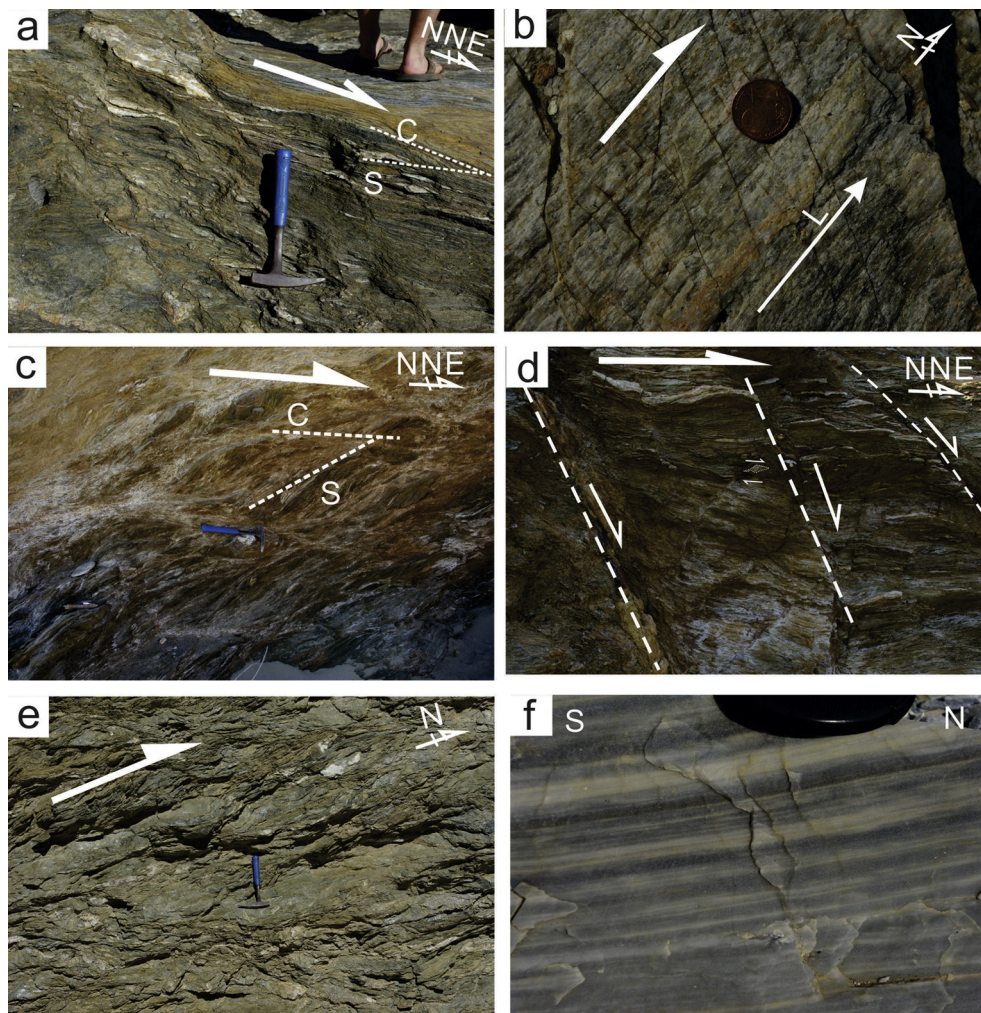
Fig. 5. Macroscopic structural evidence of deformation, observed in the Moutsounas shear zone on top of the Naxos MCC. (a) Micaschist with mylonitic foliation and stretching lineation viewed on foliation surface. Shear bands (S–C fabrics) indicating top-to-the-north shear. (b) Quartzite mylonites with a well-developed stretching lineation. (c) S–C fabrics indicating top-to-the-north shear in the mylonitic phyllite. (d) Shear fabrics with shear bands in the schist and late-stage semi-ductile top-to-the-north shear-extensional normal fault filled with quartz. (e) Foliation boudinage and top-to-the-north shear bands in the greenschist facies mylonitic schists. (f) Mylonitic calcite marble with pronounced foliation.

Naxos MCC but exclusively from the ophiolitic hanging wall unit. Miocene conglomerates, mudstones and sandstones are exposed on the northern and southern edge of the Moutsounas Peninsula (Vanderhaeghe et al., 2007). Their bedding is variable in orientation but generally dips toward the NW and oblique to the E-dipping detachment fault. Outcrop-scale faults also dip to the east. The Miocene succession is overlain by subhorizontal or gently W-dipping conglomerates of suggested Pliocene age that form the main portion of the Moutsounas peninsula and which contain numerous clasts, mainly marble, derived from the MCC. The Pliocene conglomerates are gently folded and are cut by numerous NW-trending and steeply SW-dipping normal faults. These sedimentary data indicate that exhumation of the Naxos MCC postdates the deposition of Miocene successions and predates Pliocene rocks.

5. Microstructures

5.1. Microstructures and textures: approach

The Early Miocene (M2) microfabrics are superimposed on earlier fabrics that formed during Eocene M1 metamorphism. For the comparison of microstructures and textures, we included also samples far outside of the retrogressed shear zone and we distinguish, therefore, three groups of rocks from the Naxos MCC (Fig. 3a and b):

Group 1: The main sample set is from the Moutsounas shear zone. The samples of the Moutsounas shear zone could represent variable overprint on Eocene M1 and Early Miocene M2 metamorphic fabrics according to metamorphic isogrades proposed by Jansen and Schuiling (1976).
Group 2: By comparison, a second sample set is represented rocks with a high-temperature migmatitic fabric within a thick aplitic dyke exposed at the northwestern margin of the migmatite dome. The migmatization has been dated at ca. 14–19 Ma (Martin et al., 2006). A description of migmatite structures is outside the scope of this paper.
Group 3: Rocks underwent high-pressure metamorphism and remained unaffected by the late-stage shearing of the Moutsounas shear zone. These rocks are mainly exposed in southern Naxos and exhibit high-pressure metamorphism (Avigad, 1998) of Eocene age (Wijbrans and McDougall, 1986, 1988). Retrogression during a subsequent stage of top-N shearing is moderate.

All thin sections of samples were cut parallel to the kinematic X–Z section, which is parallel to the stretching lineation and normal to the foliation.

5.2. Moutsounas shear zone (Group 1)

Microstructural investigations were concentrated on the mylonitic quartzites, micaschists and calcite-marbles from the Moutsounas shear zone.

5.2.1. Mylonitic schists and quartzitic phyllites

Core-mantle structures of quartz present a bimodal grain-size distribution that change gradually to a completely dynamically recrystallized microstructure. Undulatory and inhomogeneous or patchy extinction, grain elongation and subgrain formation are common in porphyroclastic quartz grains (Fig. 6a). The quartz porphyroclasts are elongated and some are fully recrystallized into fine-grained elongated crystals that locally show well-developed individual grain shape alignment oblique to the mylonitic layering (Fig. 6b). In some samples, quartz grains are highly recrystallized, where fewer porphyroclasts are present (Fig. 6c–h).

Polycrystalline and elongated quartz aggregates are common due to recrystallization. The preferred grain shape alignment (S_b) is oblique to the foliation (S_a) (Fig. 6c). The obliquity between foliation and S_b ranges between 5 and 35° in Type II S–C mylonites (Lister and Snoke, 1984). The most abundant quartz grains show irregular, lobate or serrated grain boundaries, which imply deformation at a relatively high temperature by grain boundary migration recrystallization (Fig. 6d and e). Locally, quartz grains also show polygonal shapes with relatively irregular or straight boundaries and 120° triple junctions (Fig. 6f), suggesting that quartz in the micaschist-quartzite underwent extensive recrystallization.

Early formed quartz microstructures were subsequently overprinted by low-temperature deformation, as evidenced by ribbon quartz grains that are partly recrystallized small-scale serration of grain boundaries, and rare occurrences of small grains in the triple junctions of larger quartz grains (Fig. 6f). Evidence for a late deformational overprint under decreasing temperature conditions is also observed in the intracrystalline microstructure, such as deformation lamellae and undulose and patchy extinction. Subgrains, as well as the deformation lamellae and deformation bands, are developed. Elongated (ribbon- or sigmoid-type) aggregates are common in the mylonites and are aligned parallel to the macroscopic foliation. Some polygonized grains occur in pressure shadows on both sides of feldspar grains (Fig. 7b and c). These have been interpreted as a major imprint by later lower temperature deformation (e.g. Brunel, 1980; Law, 1986), that likely correlates with the formation of bulging recrystallization (BLG) at greenschist-facies metamorphic conditions. A similar overprint also occurs in the southeastern part of the shear zone, where the low-temperature recrystallization of quartz occurs along discrete shear surfaces crosscutting the high-temperature deformation fabric. Microstructures also show obvious micro-faults and intragranular microfractures overprinting plastically deformed and recrystallized quartz porphyroclasts in the quartzite samples (e.g. Fig. 6a) at high angle to foliation planes. These microfractures are mostly restricted to a single grain within quartz ribbon or porphyroclastic grains, where they are approximately normal to the basal plane.

Feldspar grains in the mylonites of the Moutsounas shear zone are characterized by crystal plastic deformation (Fig. 7). In the shear direction, feldspar porphyroclasts are elongated and lenticular in shape with irregular and serrated grain boundaries. Some feldspar grains are extremely elongated and flattened into foliation, with aspect ratios of more than 5:1, and with long axes parallel to lineation (Fig. 7a). Undulatory and inhomogeneous extinction are common in porphyroclastic feldspar grains. In places, irregular grain boundaries are surrounded by a matrix of recrystallized feldspar grains. Recrystallization occurs around porphyroclasts with asymmetric fabrics, indicating a sinistral or top-to-the-north shear sense (Fig. 7b and c). Elongated porphyroclasts, as well as the cores of many mantled augens, show little evidence of internal deformation. In contrast, semi-brittle microstructures are characterized by the microfractures in some feldspar porphyroclasts. Microfractures often have infillings of quartz and mica grains (Fig. 7a–d).

White mica grains in the mylonitic schists are 50–200 μm long and a few tens of micrometers thick. The white mica matrix crystals are oriented the mylonitic foliation and lineation in the shear zone (Figs. 6e, 7a–c, e, f). Two types of white mica grains exist: coarse grains are randomly distributed in the rock and have a weak shape-preferred orientation, and fine grains are generally concentrated in small-scale (centimeters to millimeters wide) shear zones, whose original shape has been extensively modified by recrystallization. In some low-strain domains, mica-fishes are parallel to the foliation, forming a typical S–C fabric. The C-planes are defined by the fine-grained white mica aggregates and obliquely shaped white
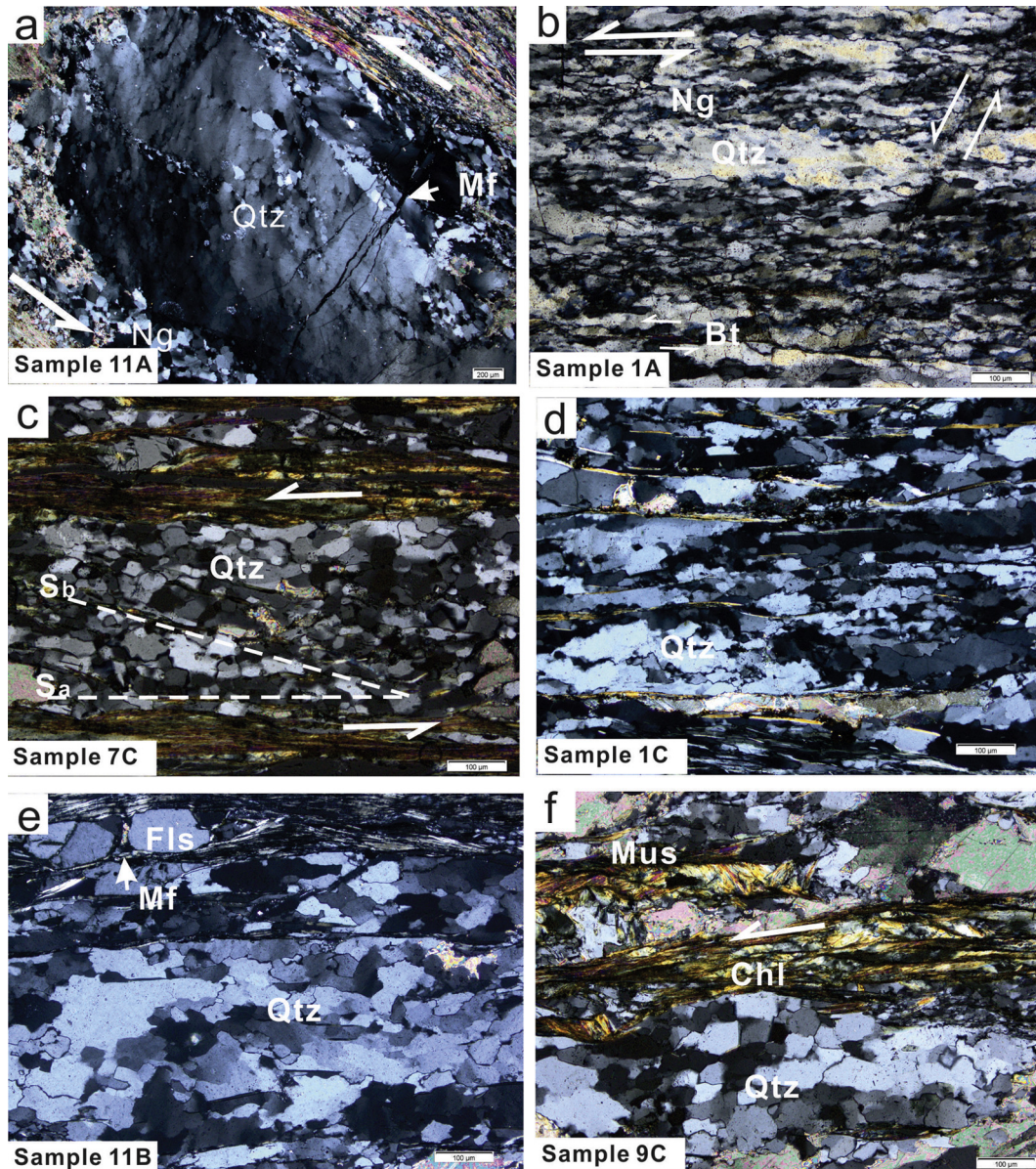
Fig. 6. Microscopic deformation characteristics of mylonitic rocks within the Moutsounas shear zone. Crossed polarized light for all photomicrographs. (a) Small dynamically recrystallized grains, subgrains and large quartz porphyroclasts in the micaschist. Elongated quartz porphyroclast displays inhomogeneous extinction. The late-stage of micro-fractures developed in the porphyroclastic grain. (b) Elongated quartz grains with polygonized shape boundaries and recrystallized aggregates. Recrystallization results in the core-mantle structure in the mylonitic quartzite. (c) Mylonitic micaschist showing angular relationships between the main (Sa) and the oblique (Sb) foliation indicating the shear sense. The Sa is mainly defined by the alignment of micaceous and flattened quartz and feldspar grains and the Sb by the shape preferred orientation of dynamically recrystallized quartz grains and mica grains. d) and (e) Elongated quartz aggregates and ribbons in quartz-rich mylonites with irregular or serrated grain boundaries by grain boundary migration recrystallization and some quartz ribbons replaced by recrystallized grains. (f) Partly annealed quartz microstructures. Quartz aggregates with relatively irregular or straight boundaries and 120° triple junctions. Sheared chlorite and white mica aggregate band. Abbreviations: Bt–biotite, Chl–chlorite, Fls–feldspar–Mf, microfracture, Mus–white mica, Ng–recrystallized new grain, Qtz–quartz.

mica with opaque mineral aggregates forming the S-planes. Some-times, opaque minerals are concentrated along the (001) planes of white mica. The primary host white mica has been progressively deformed by recrystallization to an aggregate of fine-grained mica neoblasts. Hence, some primary grains cannot longer observed optically.

Calcite grains in mylonitic calc-phyllites are variably elongated and show grain boundaries ranging from straight to diffuse and irregular (Fig. 7g) and later fine recrystallized grains occur around elongated relict grains producing a typical core-mantle structure. Twins and undulose extinction are conspicuously absent in these calcite grains. Some larger grains preserve several sets of twins or polyphase twinnings (twins in twins) at different angles, poten-tially indicating multiple deformations. Type III and Type IV twins (Ferrill et al., 2004) are common and only occur in large grains, which have not undergone complete recrystallization, and record, therefore, evidence of earlier deformation at higher temperature. However, most calcite twins are thin and straight, similar to type I and type II of Ferrill et al. (2004), and thus these are likely related to low-temperature deformation. In some samples, the elongation of calcite grains and rotation of initial twins into parallelism with the orientation of foliation. Their disc-shape appearance is consistent with pressure solution, strongly enhanced at the quartz/mica interface to calcite.
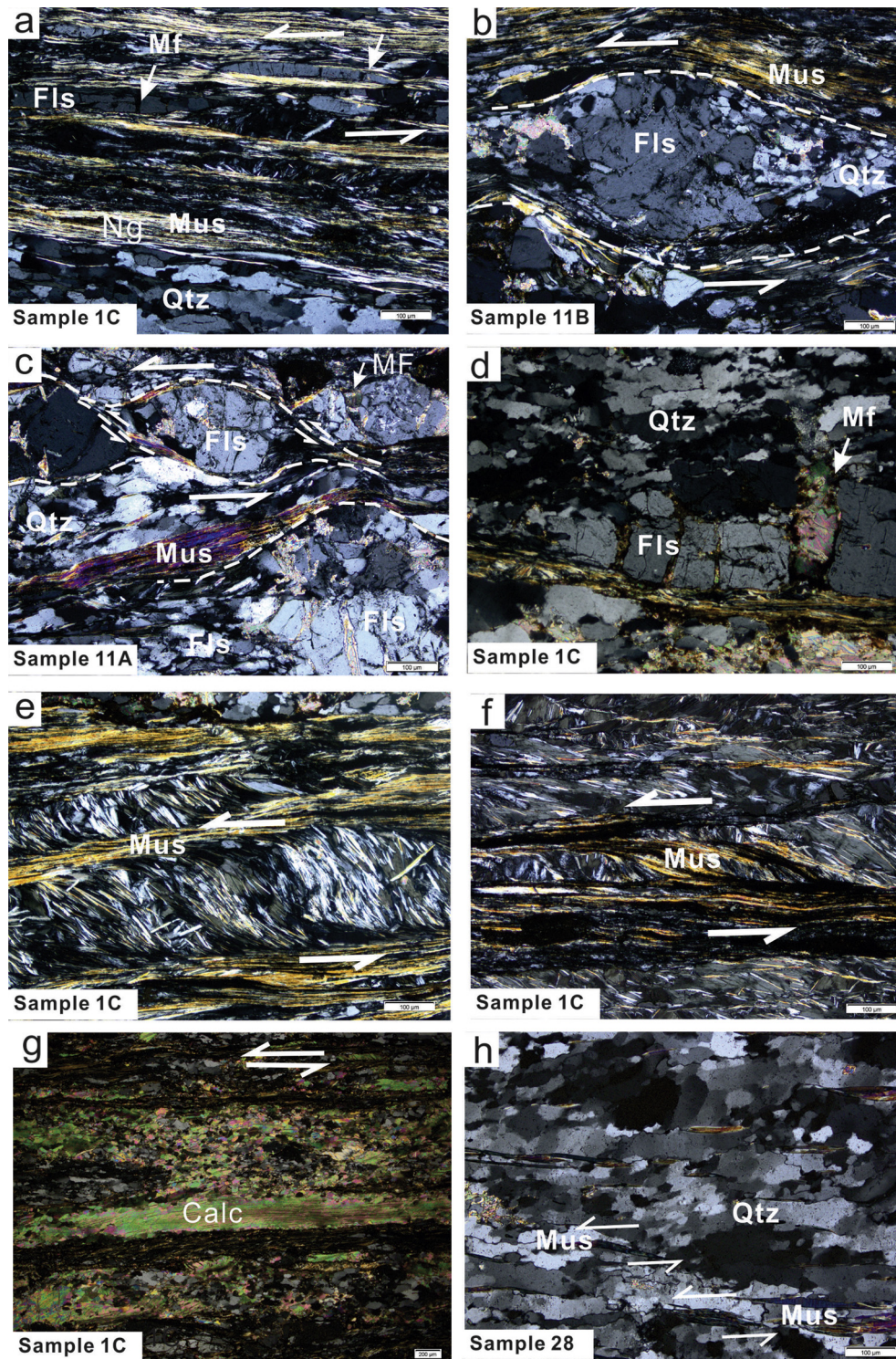
Fig. 7. Microscopic deformation characteristics of mylonitic rocks. (a) − (g) are from the Moutsounas shear zone except (f), which is from the southern high-pressure belt. (a) Extremely elongated feldspar and recrystallized muscovite oriented parallel to the stretching lineation. (b) and (c) Feldspar porphyroclasts with asymmetric fabrics, indicating top-to-the-north shear sense. (d) Feldspar elongated with late stage extensional fractures oriented perpendicular or sub-perpendicular to the stretching lineation, which is filled by muscovite, quartz and calcite. (e) and (f) Recrystallized muscovite in the matrix oriented along the defined mylonitic foliation and lineation, S−C fabrics indicating the shear sense. (g) Extremely elongated calcite grain with straight to diffuse and generally irregular grain boundaries. (h) Quartz ribbons or aggregates with serrated or sutured grain boundaries. For abbreviations, see Fig. 6. Calc−calcite.

5.2.2. Mylonitic calcite marble

Fine-grained microstructures of calcite within the ultra-mylonites are characterized by complete recrystallization with only a few porphyroclasts remaining that have straight to slightly

irregular grain boundaries (Fig. 8a−c). The recrystallized grains are slightly elongate or sub-equant. These ultramylonites are micro-structurally more homogeneous than other types, and consist of very fine-grained calcite grains. The microstructure of mylonitic

marble is typical of low-strained mylonite where porphyroclasts are abundant and appear completely surrounded by dynamically recrystallized grains producing a typical core-mantle structure (Fig. 8d–f). The coarse grains are characterized by undulatory extinction and kinking, both indicators of plastic deformation (Fig. 8e). Twins are widespread with regular as well as irregular shapes. Most twins are oriented anticlockwise to the long axis of the porphyroclasts and generally terminate at grain boundaries. Twinning systems intersect each other and some polyphase twins are common. Thick bent or curved twins inside the coarse-grained calcite likely formed during the first stages of deformation and were rotated toward parallelism with the shear zone boundary during further strain (Fig. 8e and f). Rotation and stretching of twinned porphyroclasts produced a very strong shape-preferred orientation with the orientation of the longer axes parallel to the lineation. Curved grain boundaries are indicative of grain boundary migration recrystallization. The presence of some subgrains also indicates that intracrystalline deformation mechanisms along with subgrain rotation were active. The microstructures suggest that the grain size reduction of calcite was predominantly the result of subgrain rotation recrystallization accompanied by twin boundary migration.

5.3. Aplitic dyke (Group 2) and high-pressure belt (Group 3)

Microstructures show strong plastic deformation of the main mineral phases in samples of the sheared aplite dyke located near internal migmatitic structure from the central portion of the Naxos (Group 2) and those from the southern part of the high-pressure (Group 3). The most common microstructure in the sheared aplitic dyke (Group 2) is the quartz ribbon. Elongated quartz grains compose quartz banding in a matrix of sheared feldspar grains. Such quartz ribbons form strong linear fabrics on the hand specimen scale. Feldspar grains have irregular forms and sub-granular shapes. They were elongated and have intragranular deformation. These evidences suggest that the rocks were deformed at high-or medium-temperature solid-state plastic deformation.
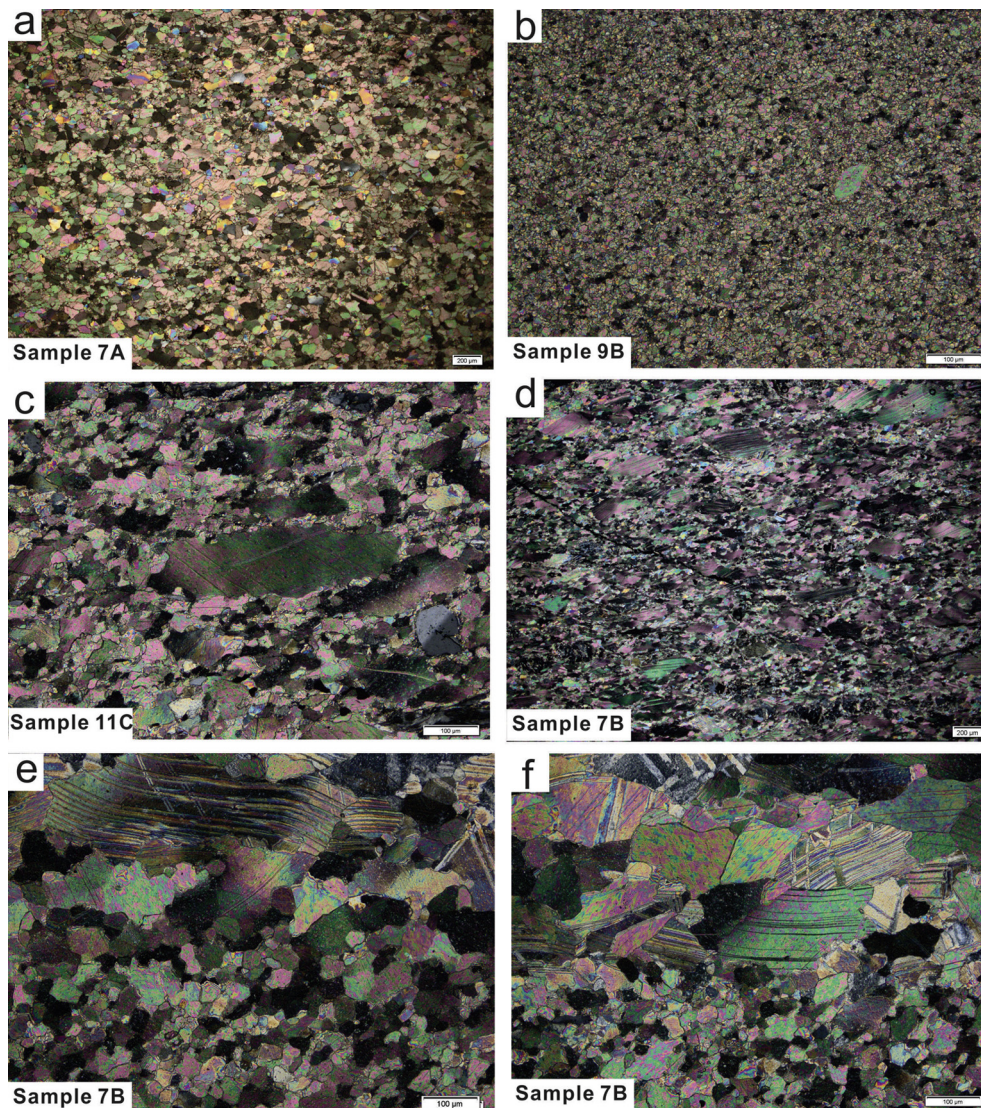
Fig. 8. Microscopic deformation characteristics of marble mylonites within the Moutsounas shear zone. (a) and (b) show completely recrystallized calcite in the ultramylonites of marble. (c) Ultramylonites with less porphyroclasts and completely surrounded by dynamically recrystallized grains producing a typical core-mantle structure. (d) Recrystallization of calcite in the mylonitic marble by subgrain rotation results in the typical core-mantle structure. (e) Twins and undulose extinction are conspicuously absent in the bent calcite porphyroclasts. (f) Polyphase twins at different angles.

In the high-pressure belt (Group 3), most quartz grains have typically polygonal aggregate shapes and are parallel or subparallel to the major foliation and lineation of the rocks (Fig. 7h). Some quartz ribbons or aggregates with serrated grain boundaries occur in pressure shadows on both sides of the feldspar grains. Some irregular or sutured grain boundaries of the quartz grains imply the dominant role of grain boundary migration recrystallization, which suggests high-temperature grain boundary migration recrystallization (e.g., Stipp et al., 2002; Passchier and Trouw, 2005). White mica is overgrown by dynamically recrystallized quartz grains. They also occur in ribbons of elongate rectangular grains or sigma-type aggregates aligned parallel to the macroscopic foliation in the mylonites. Localized low-temperature microstructures are observed, as undulatory extinction in some of the recrystallized quartz grains indicates a progressive deformation increment after their recrystallization.

6. Crystallographic preferred orientations (CPOs)

6.1. EBSD method

Crystallographic preferred orientations (CPOs) were measured using an electron-backscatter diffraction (EBSD) detector mounted on a tungsten filament Hitachi S-3400N-II scanning electron microscope (SEM) at the China University of Geosciences, Beijing (Liu et al., 2012). Detailed optical microstructural observations and CPO analysis were conducted on thin sections. All thin sections were cut parallel to the kinematic XZ plane (X — parallel to lineation, Y — parallel to foliation and normal to lineation, and Z — normal to foliation). Highly polished thin sections were prepared without cover and polished using a colloidal silica suspension with a particle size of 500 nm for 1—3 h. Thin sections were put in the scanning electron microscope chamber at a 70° tilt angle with the rock lineation (structural X reference direction) parallel to the SEM X-axis. The electron backscatter patterns were acquired at a low acceleration voltage of 15 kV and a beam working distance of ca. 18—20 mm. Conducting resin tapes attached to the sample surface surrounding the measurement area were used to reduce charging effects. The EBSD data acquisition was done using both point scan and mapping modes. Indexing was accepted when at least six detected kikuchi bands matched with those in the standard reflector file for the analyzed mineral phases and indexed points with a Mean Angular Deviation (MAD) larger than 1.2 (between detached and simulated patterns) were eliminated to avoid suspicious indexing. EBSD analysis was completed using the HKL Channel 5 software package. Pole figures were plotted in lower hemisphere equal area stereographic diagrams with the trace of the mylonitic foliation (S) and the stretching lineation (L) as reference directions. Systematic mis-indexing were noted in automated orientation maps and such data was replaced by zero solution pixels. A detailed description of the EBSD technique can be found in, e.g., Prior et al. (1996).

6.2. Quartz CPOs

CPOs of quartz were investigated mainly on mylonitic quartzite, micaschists and calcite-schists from the Moutsounas shear zone (Fig. 9, Group 1). For reference, we also analyzed textures of the quartz outside of the shear zone from the sheared aplite dyke with internal migmatitic structure (sample 24; mylonitic gneiss) (Group 2) and the southern part high-pressure belt (sample 33A, mylonitic micaschist) (Group 3) in order to compare them with textures within the Moutsounas shear zone. The volume fraction of quartz in these samples mostly varies

from 40 to 90 percent. All textures of quartz were measured from the homogenously distributed areas. The quartz measurements from these samples result in different c-axis patterns that reflect different quartz microstructures. The primarily observed c-axis distributions can be broadly classified into four main types of fabric. These are: (1) Y maxima, (2) crossed girdles, (3) single girdles, and (4) weak girdles plus dispersion. The results of the textures are depicted in Fig. 9.

Group 1: Moutsounas shear zone (Miocene)

A well-developed quartz c-axis crossed girdle pattern occurs in quartzite mylonite (sample 1C), which is characterized by a maximum in the centre (Y) and the weaker maxima distributed on a great circle (XZ), between the maximum, with a large opening angle of 65° and a smaller opening angle of 20° and 45°. The fabric patterns are also commonly held indicative for high to middle temperature deformation with a dominant combined prismatic <a> and rhomb <a> slip (e.g. Schmid and Casey, 1986). The weak submaxima were attributed to a low-temperature superimposition during subsequent deformation. The fabrics are ascribed to a basal <a> slip during low-temperature non-coaxial deformation (Stipp et al., 2002), which is consistent with microscopic observations. The quartz c-axes crossed girdle patterns are also observed in quartzitic mylonites (samples 7C and 9C). A weak maximum is close to Y and double maxima are distributed on a great circle with a 35° opening angle (sample 9C). The girdle fabric in sample 7C presents maxima in the XZ-plane at an intermediate orientation to X and Z. The patterns indicate activity of basal <a> slip and weak rhomb <a + c> slip systems with less frequent prism <a> slip, suggesting a strong low-temperature deformation overprint on a medium-temperature deformation. Asymmetric single girdle fabrics passing through the Y-direction are observed in the mylonitic quartzite (sample 1A) and micaschist (sample 11A). The concentrations of c-axes are close to the Z-axis. The girdle patterns show clockwise rotation with respect to the XZ plane. In contrast to the patterns of the other samples, these patterns here suggest dominant activation of the <a> basal slip of the deformation at lower temperatures, possibly under greenschist facies conditions. These patterns are slightly asymmetric, recording a significant component of noncoaxial deformation, consistent with top-to-the-NNE sense of shear.

Group 2: Aplitic dyke near migmatite dome (Miocene)

Quartz c-axes with Y-axis maximum fabrics are observed in the mylonitic aplitic gneiss (sample 24) from the north-western part of the MCC, with strong stretching lineation, as well as in fewer samples taken from the core of MCC. The a-axes present maxima in the XZ-plane. This configuration of c-axis point maxima to the Y-direction displays prismatic <a> slip toward a co-axial deformation. Such a situation can have resulted from high-temperature deformation under amphibolite-facies metamorphic conditions.

Group 3: High-pressure belt (Eocene)

Well-developed quartz c-axes crossed girdle pattern occurs in mylonitic micaschist (sample 33A), which presents a maximum in the centre (Y) and weaker maxima with large opening angles distributed on a great circle (XZ) (with an opening angle of 70°). The patterns are also commonly indicative of high- to medium-temperature deformation with a dominant prism<a> and rhomb <a> slip. The pattern is also asymmetric and records a significant component of non-coaxial overprint deformation, consistent with top-to-the-NNE sense of shear.
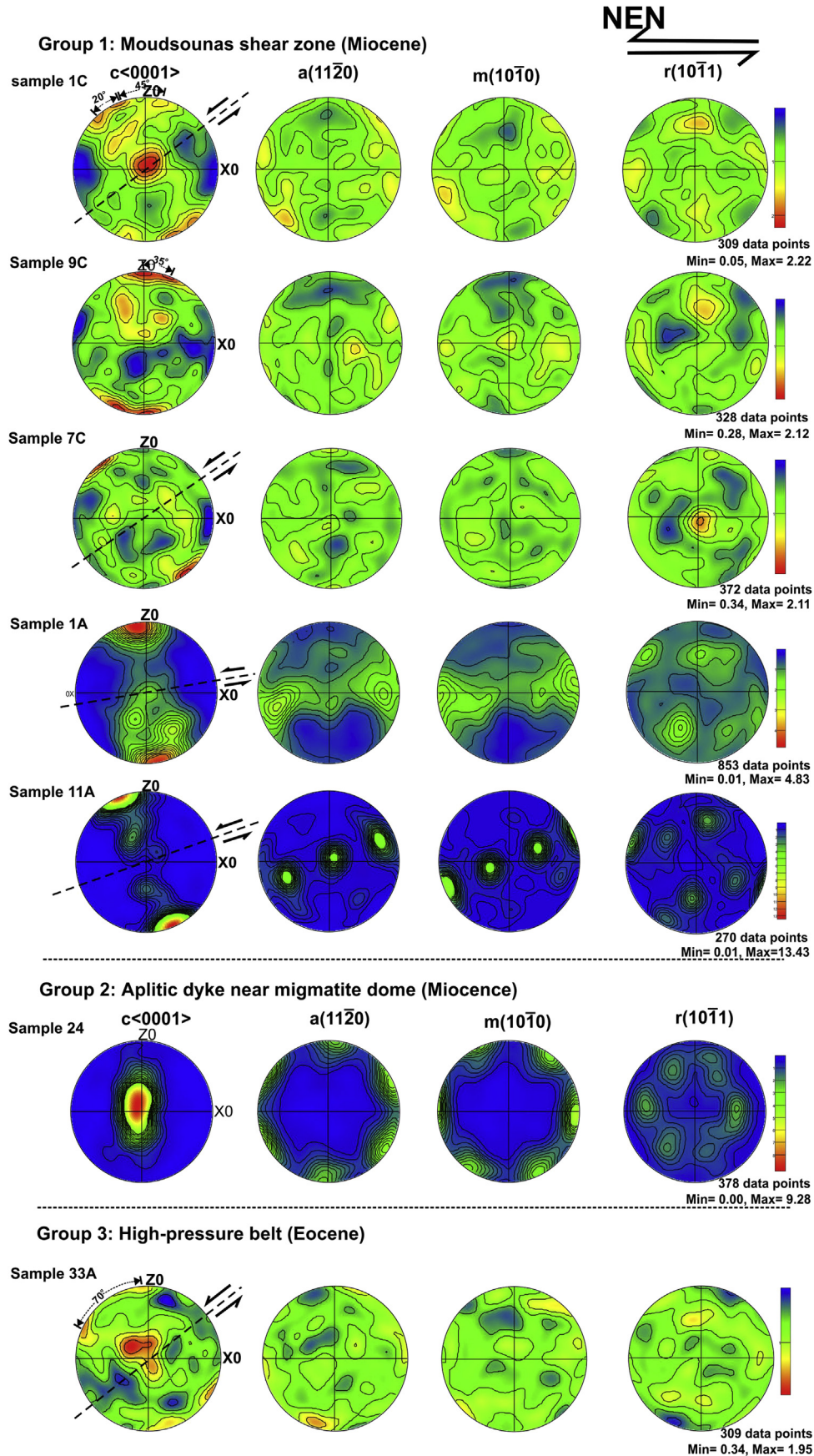
Fig. 9. EBSD measured quartz textures from the mylonitic rocks. Equal area projections, lower hemisphere, contoured at interval uniform distribution. Foliation is horizontal and lineation is in the plane in the E—W direction. The number of quartz analysis (*n*) in each sample is shown.

6.3. Calcite CPOs

C-axis textures and microstructures in calcite marble samples from the Moutsounas shear zone (Group 1), which were sheared and extensively recrystallized under greenschist facies conditions, were analyzed. All samples of calcite textures were chosen to represent within the Moutsounas shear zone (Group 1). Samples comprise: 1) ultramylonites completely dominated by dynamically recrystallized grains (Group 1a, samples 1D, 7A, 7C, 10C, 11C, 9B); and 2) mylonites characterized by core-mantle textures with oblique porphyroclasts (Group 1b, samples 5C, 6C, 7B, 7D); 3) mylonitic calcite-schists (Group 1c, samples 1C, 11A, 9C). CPOs analyses of calcite reveal variable pattern types in these samples and a different orientation of the fabric elements. Results of calcite CPO patterns are shown in Figs. 10 and 11.

Group 1a: Calcite CPOs of ultramylonites

The CPOs of ultramylonite samples (Fig. 10) show a fully orthorhombic symmetry with respect to the shear plane, with a classical broad c-axis $-<0001>$ maximum oriented normal to the stretching lineation and shear plane (XY), an a-axis girdle parallel to the shear plane with a higher abundance in the stretching lineation. E-planes (f-twin) poles exhibit a weak single maximum similar to the c-axis perpendicular to the foliation plane and stretching lineation (Fig. 10). The {r} pole plot displays a weak maximum and a broad girdle parallel to the $<c>$ poles. The CPO patterns of samples 9B and 10C display a monoclinic fabric with a c-axis distribution oblique to the shear plane. Asymmetric c-axis point maxima are rotated with respect to the shear plane, which gives a sinistral sense of shear for these samples in agreement with the general kinematics of the shear zone. The a-axes display
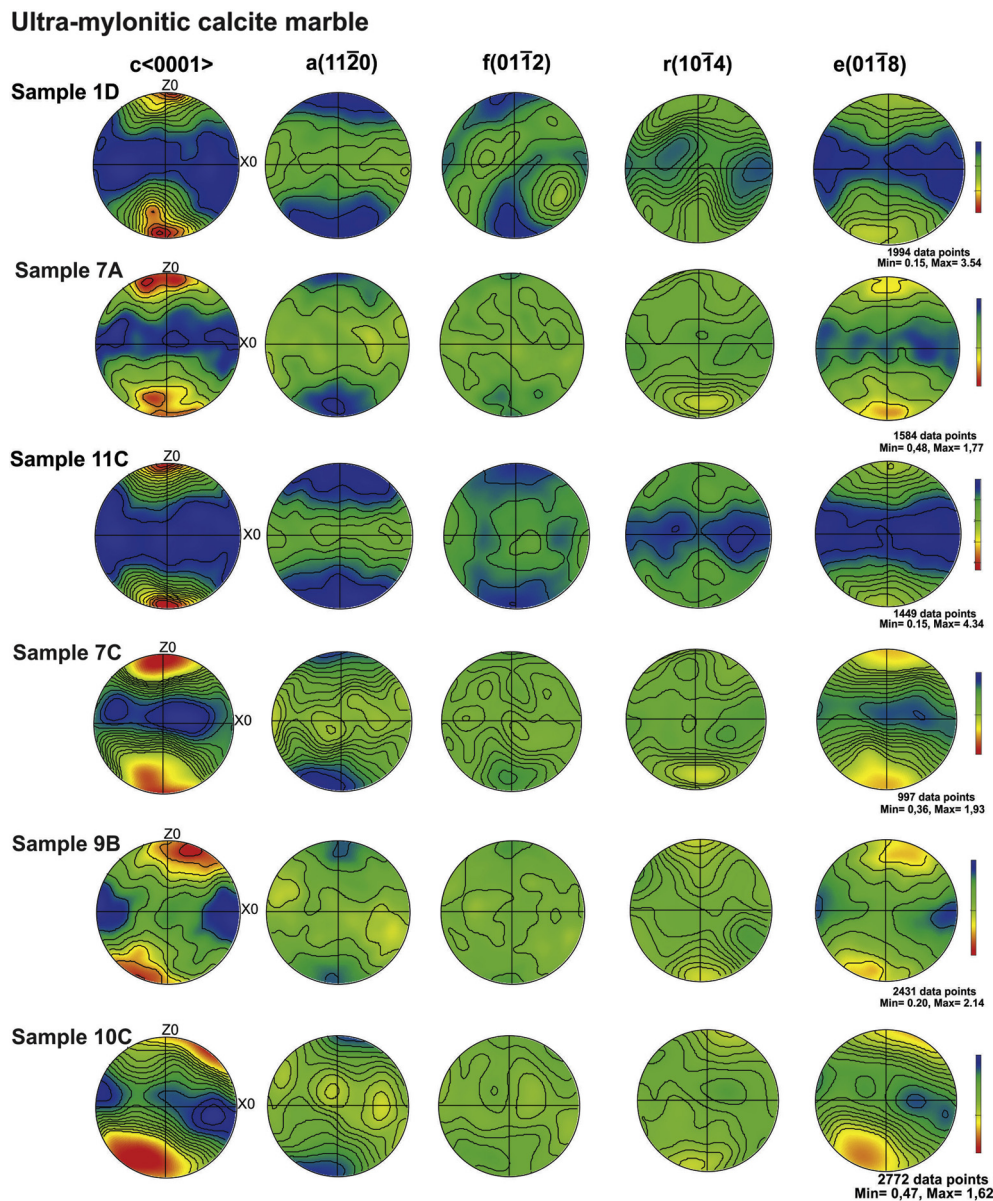
Fig. 10. EBSD measured calcite textures from the mylonitic rocks. Equal area projections, lower hemisphere, contoured at interval uniform distribution. Foliation is horizontal and lineation is in the plane in the E−W direction. The number of calcite analysis (n) in each sample is shown.

Mylonitic calcite marble with fined-porphyroclasts
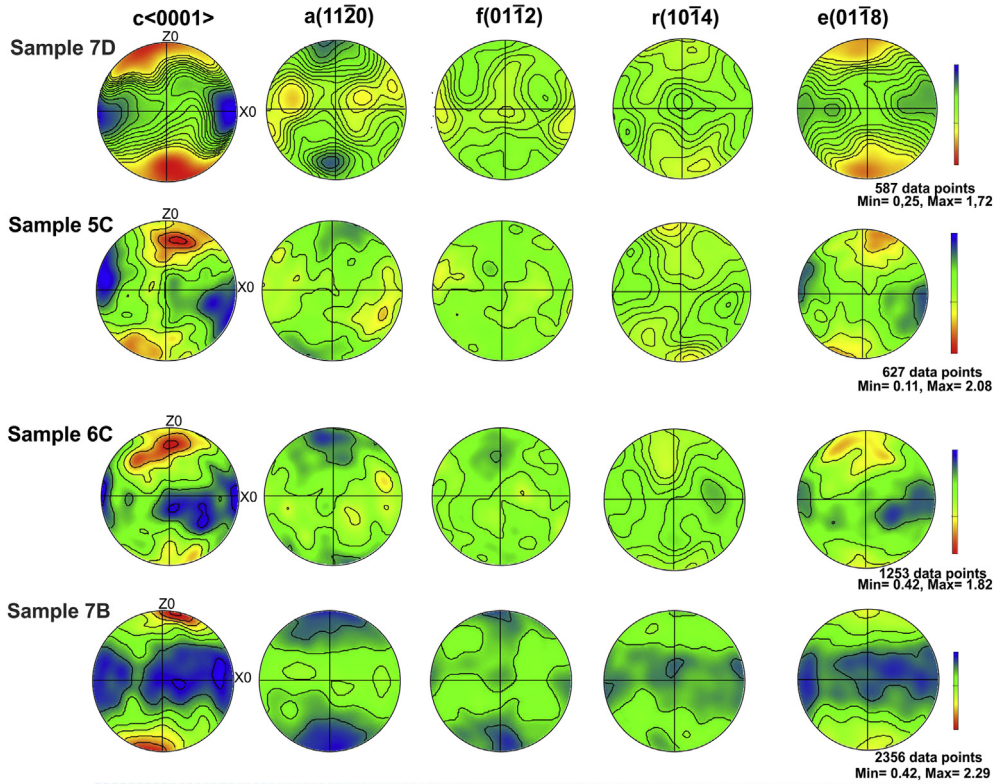
Mylonitic calcite-schist
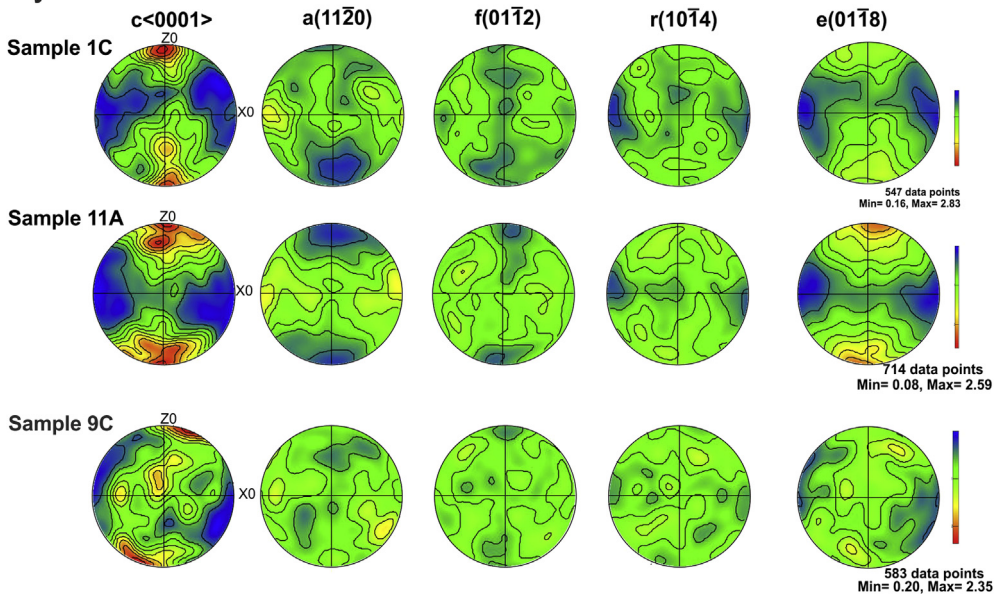
Fig. 11. Contoured diagrams of calcite grain texture data of the marble mylonites and mylonitic micaschists.

a weak broad girdle perpendicular to the main <c> maximum and show three prominent clusters within the shear plane (XY). The {r} pole plot displays a weak maximum and a broad girdle parallel to the <c> poles. The e-planes (f-twin) poles exhibit a weaker single maximum similar to the c-axis pole plot. The most suitable slip system that can be deduced from this CPO is c<a> accompanied by e<a>.

Group 1b: Calcite CPOs of low-strained mylonites

CPOs are characterized by a c-axis- <0001> maximum normal or subnormal to the shear plane accompanied by a weaker girdle of c-axis in or close the YZ plane (Fig. 11). The <a> axes are distributed within a girdle in or close to the XY shear plane with a maximum in the X-direction. The f <e>-twin poles are weakly distributed on a

similarly oriented axis. The CPO patterns with a c-axis distribution are oblique to the shear plane. The c-axis point maximum rotated opposite to the sense of shear, and consequently the asymmetry of the c-axis point maximum with respect to the shear plane is a shear sense indicator.

Group 1c: CPOs of calcites from mylonitic calc-schist

CPO exhibits a weak c-axis girdle distribution around the lineation (in the YZ plane) with a c-axis- <0001> maximum close to the Z-axis of finite strain (Fig. 11). The pole figures of the a-axis girdle is oriented parallel to the shear plane and the f-twin poles are weakly distributed on a similarly oriented axis. The calcite grains underwent continuous internal deformation and rotation during shearing, which produced a monoclinic CPO and, consequently, the asymmetry of the c-axis point maximum with respect to the shear plane is a shear sense indicator.

7. Thermobarometric calculations

Beside white mica, chlorite is one of the most common minerals formed during very low-grade and low-grade metamorphism (especially in greenschist facies) to moderate thermobarometric conditions (150—450 °C, and up to a few kilobar) (Cathelineau and Nieva, 1985, Cathelineau, 1988). To get constraints on the temperature conditions of deformation during the high-pressure (M1) metamorphism that proceeded overprinting thermal metamorphism (M2), and especially during shearing and cooling, thin polished sections were prepared from the Moutsounas shear zone

and high-pressure rocks for the analysis of chlorites and white mica.

7.1. EPMA methodology

Electron microprobe analysis (EMPA) of white mica and chlorite were carried out on a JEOL electron microprobe (JXA-8600) at the Department Geography and Geology, University of Salzburg, using a wavelength dispersive system. We used an acceleration voltage of 15 kV and a sample current of 40 nA. Natural and synthetic mineral standards were used to calibrate the microprobe and raw data was reduced using standard ZAF correction. The detection limits (2σ) for the elements Si are Al are 0.06 wt% and 0.04 wt%, respectively, for Na, K, Mg, Mn, and Fe are 0.025 wt%. Table 2 shows selected results of individual analyses of white mica and Table 3 show the results for chlorite including calculated temperatures (see below). Structural formulae have been calculated on the basis of 28 oxygens for chlorites, and of 22 oxygens for white mica. Three different types of composition chlorite geothermometers were applied in this work: (1) geothermometer of Cathelineau (1988) (T1) based on the number of tetrahedral Al; (2) geothermometers of Kranidiotis and MacLean (1987) (T2) and Jowett (1991) (T3) based on the number of tetrahedral Al and the value Fe/(Fe + Mg). The Cathelineau (1988) (T1) equation yields results very similar to the Kranidiotis and MacLean (1987) and Jowett (1991) methods (Table 3, results of geothermometers T1, T2 and T3, respectively).

We also applied phengite barometry on white mica based on the experimental calibration of Massonne and Schreyer (1987, 1997) because of the potential preservation of phengite-rich white mica

Table 1
List of investigated samples and methods applied to individual samples. Group 1, 2, 3 refers to structural units as defined in the main text. EBSD, electron back-scattered diffraction; EPMA, electron microprobe analysis.

Sample no.	Rock type	Group	Longitude	Latitude	Microstructures	EBSD texture	Paleopiezometry		EMPA	
							Quartz	Calcite	White mica	Chlorite
NAX-1A	Mylonitic quartzite	Group 1	37° 05′00.7″	25° 35′17.9″	x	Quartz	x		x	x
NAX-1B	Mylonitic marble	1			x					
NAX-1C	Mylonitic phyllite	1			x	Quartz, calcite	x		x	x
NAX-1D	Ultramylonitic calcite-marble	1			x	Calcite		x		
NAX-2A	Mylonitic marble	1	37° 04′46.8″	25° 35′20.9″	x					
NAX-5C	Mylonitic marble	1			x	Calcite				
NAX-6C	Mylonitic marble	1	37° 05′00.7″	25° 34′35.5″	x	Calcite				
NAX-7A	Ultramylonitic marble	1			x	Calcite		x		
NAX-7C	Ultramylonitic marble	1	36° 59′43.0″	25° 33′46.3″	x	Quartz	x		x	x
Nax-7D	Mylonitic marble	1			x	Calcite				
NAX-7B	Mylonitic marble	1			x	Calcite		x		
NAX-8	Mylonitic phyllite	1	36° 57′34.8″	25° 32′14.7″	x					
NAX-9A	Banded sericite quartzite	1	36° 57′48.3″	25° 33′01.7″	x				x	
NAX-9B	Ultramylonitic marble	1			x	Calcite		x		
NAX-9C	Mylonitic quartzphyllite	1			x	Quartz, calcite	x	x	x	x
NAX-10c	Ultramylonitic marble	1	36° 58′28.5″	25° 35′26.1″	x	Calcite		x		
NAX-11A	Micaschist	1	37° 05′24.5″	25° 35′30.0″	x	Quartz, calcite	x			
NAX-11B	Sheared quartzitic phyllite	1			x		x		x	x
NAX-11C	Ultramylonitic marble	1			x	Calcite		x		
NAX-17A	Ultramylonitic schist	1	37° 05′43.4″	25° 26′14.4″	x					
NAX-17B	Calcite marble	1			x					
NAX-24	Mylonitic aplite gneiss	Group 2	37° 28′31.0″	25° 27′59.6″	x	Quartz				
NAX-28	Quartz-bearing micaschist	Group 3	36° 56′06.1″	25° 28′30.3″	x		x			
NAX-29A	Micaschist	3	36° 56′16.43″	25° 28′26.9″	x				x	x
NAX-29C	Quartzitic micaschist	3			x		x			
NAX-33A	Phyllonitic micaschist	3	36° 58′13.6″	25° 28′53.4″	x	Quartz	x			
NAX-33B	Quartzitic micaschist	3			x		x			

Table 2
Representative compositions of white mica.

Sample no.	29A-1	29A-2	29A-3	29A-4	29A-5	29A-6	29A-7	29A-8	29A-9	29A-10	29A-11	29_12	1C-2	1C-3	1C-4	7C-2	7C-3	7C-4	7C-5	7C-6	7C-7	7C-10
Chemical composition (wt. %) (assuming 22 oxygen)																						
SiO_2	48.81	48.36	49.67	48.28	49.94	50.40	49.34	49.55	50.03	50.03	48.53	47.57	45.54	45.75	50.74	49.23	48.34	47.75	49.33	49.84	51.99	47.21
Al_2O_3	25.49	28.12	25.75	26.50	26.15	25.31	25.55	25.63	25.88	25.99	28.66	29.96	24.64	25.53	25.27	24.01	24.00	24.66	23.33	23.74	23.45	23.06
MgO	2.65	2.32	2.71	2.68	2.86	2.96	2.67	2.64	2.75	2.88	2.23	1.92	5.60	4.36	3.50	3.90	4.01	4.79	4.85	4.97	4.10	5.45
Na_2O	0.19	0.27	0.14	0.26	0.19	0.21	0.13	0.17	0.30	0.26	0.30	0.50	0.19	0.35	0.12	0.14	0.16	0.20	0.10	0.10	0.07	0.18
CaO	0.09	0.13	0.02	0.18	0.05	0.02	0.12	0.00	0.00	0.00	0.05	0.06	0.06	0.07	0.02	0.12	0.15	0.17	0.08	0.09	0.00	0.10
TiO_2	0.19	0.25	0.14	0.25	0.14	0.18	0.22	0.17	0.25	0.21	0.20	0.11	0.18	2.32	0.12	0.20	0.19	0.19	0.21	0.16	0.14	0.15
FeO	3.41	2.74	3.10	2.86	2.77	3.37	3.17	3.34	3.09	2.76	2.08	1.88	4.89	3.46	2.03	3.59	3.51	4.86	4.11	3.99	2.90	4.93
MnO	0.00	0.00	0.03	0.01	0.06	0.00	0.00	0.04	0.01	0.00	0.01	0.00	0.00	0.00	0.00	0.02	0.06	0.02	0.05	0.08	0.03	0.06
Cr_2O_3	0.00	0.02	0.03	0.01	0.02	0.02	0.03	0.01	0.01	0.00	0.00	0.01	0.16	0.17	0.11	0.08	0.06	0.10	0.05	0.11	0.23	0.12
K_2O	10.44	10.12	10.45	10.32	10.35	10.53	10.26	10.60	10.44	10.34	10.38	9.96	8.11	8.17	10.33	8.60	7.77	7.04	8.79	9.01	10.49	7.71
Total	91.28	92.33	92.04	91.35	92.53	92.99	91.49	92.15	92.76	92.47	92.44	91.98	89.36	90.19	92.25	89.92	88.19	89.82	90.93	92.04	93.43	89.00
Structural formulae on the basis of 22 negative charges																						
Si	6.85	6.67	6.89	6.76	6.87	6.93	6.89	6.88	6.89	6.89	6.67	6.56	6.55	6.48	6.97	6.95	6.92	6.75	6.92	6.91	7.09	6.78
Al	4.22	4.57	4.21	4.37	4.24	4.10	4.20	4.20	4.20	4.22	4.64	4.87	4.18	4.26	4.09	3.99	4.05	4.11	3.86	3.88	3.77	3.91
Mg	0.55	0.48	0.56	0.56	0.59	0.61	0.56	0.55	0.56	0.59	0.46	0.39	1.20	0.92	0.72	0.82	0.86	1.01	1.01	1.03	0.83	1.17
Na	0.05	0.07	0.04	0.07	0.05	0.06	0.03	0.04	0.08	0.07	0.08	0.13	0.05	0.10	0.03	0.04	0.04	0.06	0.03	0.03	0.02	0.05
Ca	0.01	0.02	0.00	0.03	0.01	0.00	0.02	0.00	0.00	0.00	0.01	0.01	0.01	0.01	0.00	0.02	0.02	0.03	0.01	0.01	0.00	0.02
Ti	0.02	0.03	0.01	0.03	0.01	0.02	0.02	0.02	0.03	0.02	0.02	0.01	0.02	0.25	0.01	0.02	0.02	0.02	0.02	0.02	0.01	0.02
Fe	0.40	0.32	0.36	0.33	0.32	0.39	0.37	0.39	0.36	0.32	0.24	0.22	0.59	0.41	0.23	0.42	0.42	0.57	0.48	0.46	0.33	0.59
Mn	0.00	0.00	0.00	0.00	0.01	0.00	0.00	0.00	0.00	0.00	0.00	0.00	0.00	0.00	0.00	0.01	0.00	0.01	0.01	0.00	0.01	0.01
Cr	0.00	0.00	0.00	0.00	0.00	0.00	0.00	0.00	0.00	0.00	0.00	0.00	0.02	0.02	0.01	0.01	0.01	0.01	0.01	0.01	0.03	0.01
K	1.87	1.78	1.85	1.84	1.82	1.85	1.83	1.88	1.83	1.82	1.82	1.75	1.49	1.48	1.81	1.55	1.42	1.27	1.57	1.59	1.83	1.41

Sample no.	7C-9	7C-11	7C-14	7C-15	7C-16	7C-17	9C-1	9C-2	9C-3	9C-4	9C-5	9C-6	9C-7	9C-8	9C-9	11B-1	11B-2	11B-3	11B-4	11B-7	11B-8	11B-9
Chemical composition (wt. %) (assuming 22 oxygen)																						
SiO_2	48.91	47.32	49.05	48.19	47.02	46.48	48.62	48.78	48.90	43.00	50.04	44.64	47.04	49.27	47.15	49.84	49.33	49.58	47.82	45.78	41.71	41.52
Al_2O_3	23.88	23.04	24.48	23.77	22.86	24.56	26.23	26.30	26.44	24.21	26.59	25.01	25.34	26.46	24.93	25.98	25.88	26.66	25.55	25.51	24.05	27.18
MgO	4.21	5.93	4.41	4.25	4.03	5.34	3.06	3.55	2.80	6.26	2.97	5.43	3.63	3.03	2.87	3.54	3.96	3.33	4.99	5.43	8.77	7.21
Na_2O	0.21	0.20	0.14	0.14	0.17	0.30	0.25	0.18	0.30	0.44	0.25	0.29	0.23	0.15	0.14	0.16	0.18	0.11	0.21	0.18	0.07	0.29
CaO	0.19	0.13	0.13	0.17	0.20	0.10	0.20	0.13	0.33	0.29	0.08	0.24	0.11	0.05	0.07	0.04	0.08	0.06	0.07	0.02	0.04	0.08
TiO_2	0.21	0.22	0.21	0.28	0.22	0.11	1.16	0.26	0.26	0.35	0.18	0.09	0.21	0.13	0.16	0.26	0.22	0.24	0.14	0.28	0.13	0.21
FeO	3.33	5.30	3.73	5.07	4.79	4.98	2.74	3.12	3.18	8.80	2.13	7.21	4.29	2.63	2.42	2.18	2.59	2.07	4.05	4.80	8.60	7.55
MnO	0.03	0.05	0.07	0.03	0.02	0.03	0.03	0.06	0.02	0.06	0.01	0.05	0.07	0.03	0.04	0.01	0.00	0.00	0.01	0.05	0.04	0.03
Cr_2O_3	0.17	0.14	0.11	0.15	0.05	0.03	0.19	0.16	0.22	0.22	0.19	0.28	0.18	0.08	0.04	0.08	0.10	0.18	0.21	0.36	0.24	0.10
K_2O	8.15	8.03	8.14	8.48	8.05	6.33	9.80	9.96	8.96	6.79	10.32	7.54	9.21	10.21	9.66	10.25	9.58	9.97	8.98	8.66	6.31	6.66
Total	89.29	90.37	90.48	90.53	87.40	88.26	92.29	92.49	91.30	90.41	92.76	90.77	90.32	92.04	87.49	92.34	91.94	92.20	92.03	91.06	89.96	90.83
Structural formulae on the basis of 22 negative charges																						
Si	6.93	6.73	6.87	6.83	6.88	6.72	6.74	6.80	6.80	6.25	6.85	6.40	6.69	6.81	6.85	6.86	6.81	6.81	6.65	6.48	6.08	5.96
Al	3.99	3.86	4.04	3.97	3.94	4.16	4.27	4.28	4.33	4.15	4.29	4.23	4.25	4.31	4.27	4.21	4.21	4.32	4.19	4.26	4.13	4.60
Mg	0.89	1.26	0.92	0.90	0.88	1.14	0.63	0.73	0.58	1.36	0.61	1.16	0.77	0.62	0.62	0.73	0.82	0.68	1.04	1.15	1.91	1.54
Na	0.06	0.06	0.04	0.04	0.05	0.08	0.07	0.05	0.08	0.13	0.07	0.08	0.06	0.04	0.04	0.04	0.05	0.03	0.06	0.05	0.02	0.08
Ca	0.03	0.02	0.02	0.03	0.03	0.02	0.03	0.02	0.05	0.05	0.01	0.04	0.02	0.01	0.01	0.01	0.01	0.01	0.01	0.00	0.01	0.01
Ti	0.02	0.02	0.02	0.03	0.02	0.01	0.12	0.03	0.02	0.04	0.02	0.01	0.02	0.01	0.02	0.03	0.02	0.02	0.01	0.03	0.01	0.02
Fe	0.39	0.63	0.44	0.60	0.59	0.60	0.32	0.36	0.37	1.07	0.24	0.86	0.51	0.30	0.29	0.25	0.30	0.24	0.47	0.57	1.05	0.91
Mn	0.00	0.01	0.01	0.00	0.00	0.00	0.00	0.00	0.01	0.01	0.00	0.01	0.01	0.00	0.00	0.00	0.00	0.00	0.00	0.01	0.00	0.00
Cr	0.02	0.02	0.01	0.02	0.01	0.00	0.02	0.02	0.02	0.02	0.02	0.03	0.02	0.01	0.00	0.01	0.01	0.02	0.02	0.04	0.03	0.01
K	1.47	1.46	1.45	1.53	1.50	1.16	1.73	1.76	1.59	1.26	1.80	1.38	1.67	1.80	1.79	1.80	1.69	1.75	1.59	1.56	1.17	1.22

Table 3
Selected data on chemistry of chlorites and calculated temperatures of formation (T1 to T3, see text).

Location	Group 3 (high-pressure belt)					Group 1 (Moutsounas shear zone)																	
Sample no.	29A-01	29A-02	29A-03	29A-04	29A-05	1C-01	1C-02	9C-01	9C-02	9C-03	9C-04	9C-05	11B-01	7C-01	7C-02	7C-03	7C-04	7C-05	7C-06	7C-07	7C-08	9C-05	9C-06
Microfabric type[a]						Type I	Type I	Type I	Type I	Type I	Type I	Type I	Type I	Type I	Type I	Type I	Type II	Type II	Type II	Type II	Type II	Type II	Type II
Chemical composition (wt. %) (assuming 28 oxygen)																							
SiO_2	25.06	25.78	25.38	25.16	25.16	26.88	26.50	26.53	27.35	26.36	25.62	26.72	26.58	28.87	28.79	27.76	29.38	28.29	29.18	28.20	27.94	30.17	29.60
Al_2O_3	20.91	20.64	20.74	21.07	21.37	19.68	19.70	19.15	19.23	19.67	19.20	19.68	20.85	18.10	17.97	17.96	17.48	17.22	16.71	17.96	15.46	18.02	19.43
MgO	14.50	14.14	14.09	14.70	14.24	17.73	17.85	15.22	14.94	16.01	15.95	15.03	18.52	17.27	16.69	17.53	17.40	16.53	15.37	17.54	13.57	13.28	13.45
Na_2O	0.00	0.03	0.05	0.04	0.01	0.02	0.04	0.10	0.12	0.08	0.07	0.11	0.07	0.22	0.41	0.11	0.49	0.39	0.67	0.15	0.71	1.07	0.63
CaO	0.03	0.06	0.13	0.04	0.20	0.07	0.07	0.35	0.14	0.15	0.29	0.17	0.21	0.16	0.37	0.39	0.45	0.49	0.56	0.14	0.50	0.53	0.54
TiO_2	0.05	0.02	0.04	0.06	0.07	0.06	0.03	0.01	0.05	0.02	0.03	0.03	0.05	0.03	0.05	0.01	0.03	0.00	0.09	0.05	0.09	0.00	0.02
FeO	24.68	25.06	25.22	25.01	24.86	19.72	20.48	21.81	21.79	22.29	22.09	22.95	19.15	19.81	19.17	19.29	18.81	19.31	21.41	19.59	19.54	20.97	20.23
MnO	0.15	0.16	0.19	0.15	0.18	0.27	0.20	0.33	0.35	0.39	0.42	0.35	0.14	0.37	0.29	0.29	0.28	0.30	0.25	0.33	0.23	0.29	0.33
Cr_2O_3	0.01	0.02	0.04	0.02	0.02	0.11	0.05	0.18	0.45	0.07	0.09	0.05	0.02	0.05	0.00	0.00	0.01	0.01	0.07	0.05	0.08	0.11	0.20
K_2O	0.00	0.00	0.00	0.00	0.00	0.00	0.00	0.00	0.06	0.00	0.00	0.00	0.02	0.00	0.00	0.00	0.00	0.00	0.07	0.00	0.30	0.21	0.00
Total	85.40	85.90	85.89	86.25	86.12	84.55	84.92	83.68	84.48	85.02	83.77	85.10	85.62	84.88	83.73	83.35	84.33	82.52	84.39	83.99	78.42	84.65	84.42
Structural formulae on the basis of 28 negative charges ($Al^{IV} = 8-Si$)																							
Al^{IV}	1.29	1.23	1.27	1.31	1.30	1.15	1.19	1.12	1.06	1.18	1.20	1.13	1.23	0.96	0.93	1.02	0.90	0.93	0.87	0.99	0.78	0.79	0.87
Si	5.41	5.54	5.47	5.39	5.39	5.70	5.62	5.77	5.87	5.65	5.59	5.73	5.55	6.08	6.14	5.96	6.20	6.14	6.26	6.01	6.43	6.42	6.27
Al	5.32	5.22	5.27	5.32	5.40	4.92	4.93	4.90	4.87	4.97	4.94	4.98	5.13	4.50	4.51	4.55	4.35	4.41	4.23	4.51	4.19	4.52	4.85
Mg	4.67	4.53	4.52	4.69	4.55	5.61	5.65	4.93	4.78	5.12	5.19	4.81	5.76	5.43	5.30	5.61	5.48	5.35	4.92	5.57	4.66	4.21	4.24
Na	0.00	0.01	0.02	0.02	0.01	0.01	0.02	0.04	0.05	0.03	0.03	0.05	0.03	0.09	0.17	0.05	0.20	0.16	0.28	0.06	0.32	0.44	0.26
Ca	0.01	0.01	0.03	0.01	0.05	0.02	0.02	0.08	0.03	0.03	0.07	0.04	0.05	0.04	0.08	0.09	0.10	0.11	0.13	0.03	0.12	0.12	0.12
Ti	0.01	0.00	0.01	0.01	0.01	0.01	0.01	0.00	0.01	0.00	0.01	0.01	0.01	0.00	0.01	0.00	0.01	0.00	0.01	0.01	0.01	0.00	0.00
Fe	4.46	4.50	4.54	4.48	4.46	3.50	3.64	3.96	3.91	3.99	4.03	4.12	3.34	3.49	3.42	3.47	3.32	3.51	3.84	3.49	3.76	3.73	3.58
Mn	0.03	0.03	0.03	0.03	0.03	0.05	0.04	0.06	0.06	0.07	0.08	0.06	0.02	0.07	0.05	0.05	0.05	0.05	0.05	0.06	0.05	0.05	0.06
Cr	0.00	0.00	0.01	0.00	0.00	0.02	0.01	0.03	0.08	0.01	0.01	0.01	0.00	0.01	0.00	0.00	0.00	0.00	0.01	0.01	0.02	0.02	0.03
Temperature (T°C)																							
T1	354	335	346	358	358	308	321	298	281	317	326	303	333	246	238	266	227	237	218	258	190	193	217
T2	328	316	324	331	331	290	299	288	277	300	306	293	305	250	245	262	236	244	235	258	217	221	236
T3	359	340	351	363	363	310	323	302	285	320	329	307	334	249	241	268	230	240	222	261	195	199	222

[a] Microfabric type in sheared samples from the Moutsounas shear zone: type I- coarse-grained microlithons; type II- sheared with very fine-grained mixtures of white mica and chlorite.

formed during the high-pressure metamorphism M1 predating the activity of the Moutsounas shear zone.

We selected five chlorite-bearing phyllitic samples for this analysis (Table 1). Sample 29A is from the high-pressure rocks (Group 3) in the southern part of Naxos, which was chosen to test the methodology. Samples 1C, 7C, 9C, 11C are from sheared low-grade metamorphic rocks (Group 1) from the surroundings of Moutsounas. Sample 11C is from the shear zone in southeastern Naxos (Group 1).

7.2. Thermometry and barometry results

We first describe results from Group 3, sample 29A (Fig. 12a). White mica and chlorite of this sample are coarse-grained and are seemingly in textural equilibrium according to the detailed back-scatter electron (BSE) images (Fig. 12). White mica shows high Si contents (atoms per formula unit − a.p.f.u.), range 6.56–6.93, with the majority of data at ca. 6.90 Si apfu; Table 2), as is expected for high pressure rocks (Fig. 13a). Application of phengite barometry on white mica at a temperature of 360 °C yields a main range of pressure ca. 8–12 kbar (Fig. 13b) in accordance with peak P of 12 kbar reported by Avigad (1998). In the Moutsounas shear zone (Group 1 samples), we observed chlorite in two microfabric types (e.g., samples 1C, 7C, 9C, 11B) (Fig. 12b and c): (1) early formed coarse-grained chlorite within microlithons, sometimes associated with white mica (Type I), and (2) very fine-grained sheared band mixtures of white mica and chlorite, with apparent disequilibrium boundaries (Type II). Chlorite thermometry yields results ranging from 320 to 360 °C (Table 3) (Fig. 14). In most cases, the chlorite geothermometers yield temperatures ca. 290–320 °C for micro-fabric Type 1, and ca. 200–260 °C for microfabric Type II. In the case of sample 7C, chlorite from coarse microlithons yields tempera-tures ranging from 190 to 268 °C, and these are lower than in other samples suggesting sub-greenschist facies conditions. White mica

yields a wide range of compositions with a dominance of Si at ca. 6.8–6.9 a.p.f.u. and has, therefore, phengitic compositions, and muscovite grains with a low Si a.p.f.u. at ca. 6.1 (Fig. 13a). Some phengitic compositions with high-Si white micas also occur in the sheared zones (microfabric Type 2) (Fig. 13a, Table 2). We note that phengite is, therefore, inherited from high-pressure meta-morphism M1, and is only rarely reset to low-pressure white mica during shearing and exhumation.

8. Palaeopiezometer

8.1. Flow stress estimate from recrystallized grain size

Based on the grain size of dynamically recrystallized quartz and calcite, the piezometer can be used to calculate the differential stress from the grain size at a given temperature (e.g., Hacker et al., 1992; Gueydan et al., 2005; Warren and Hirth, 2006; Austin and Evans, 2007; Mehl and Hirth, 2008; Okudaira and Shigematsu, 2012). Under the obtained differential stress conditions, the strain rate can be estimated. The piezometers used were established for quartz (Twiss, 1977; Mercier et al., 1977; Koch, 1983; Stipp and Tullis, 2003; Stipp et al., 2010) and for calcite (Rutter, 1995). A suite of previously described quartzite, quartz-rich schists and calcite marbles of the Moutsounas shear zone were used for paleo-piezometric analysis. The samples are representative of syntectonic microstructures. For the present study, only samples with a uni-form recrystallized grain size were considered for paleostress estimation. The diameters of equant recrystallized grains were measured optically on a standard petrographic microscope (for details, see also Behrmann and Seckel, 2007). Each grain was measured parallel and perpendicular to the macroscopic foliation. A minimum of 80 grains were measured in each sample. The mean grain size is calculated using the formula of Behrmann (1985). The results of analysis and differential flow stresses from dynamically
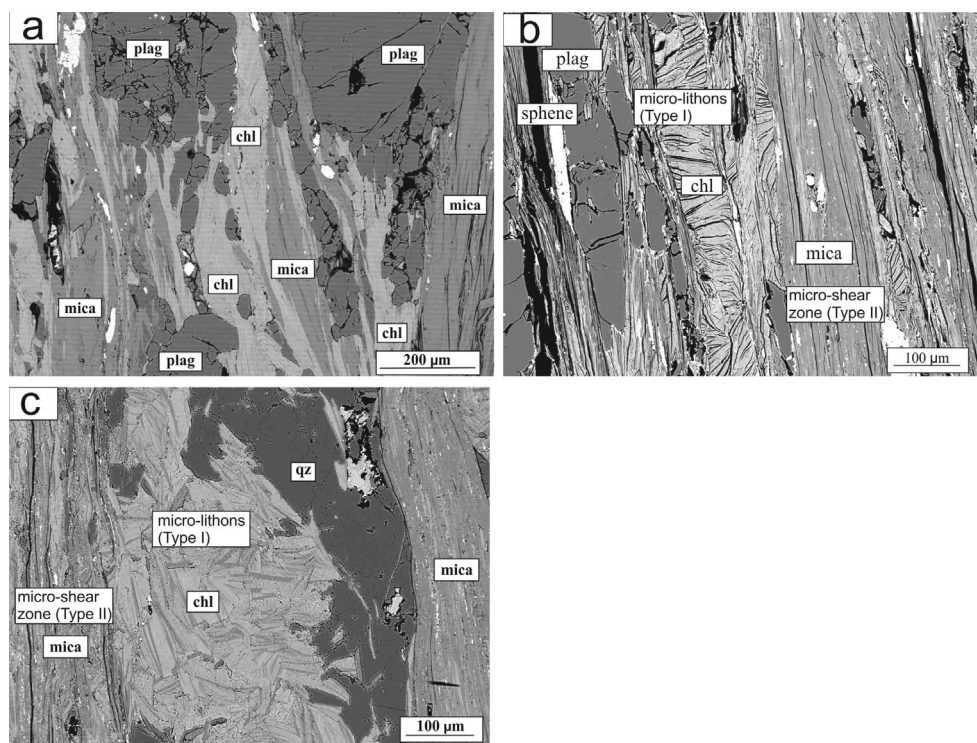
Fig. 12. Back-scatter electron microscopy images of microfabrics containing white mica and chlorite: (a) Fabric dominated by high-pressure metamorphic overprint M1 (Group 3, sample 29A). (b) and (c) are representative sheared phyllitic rocks from the Moutsounas shear zone (Group 1, samples 7C and 1C).
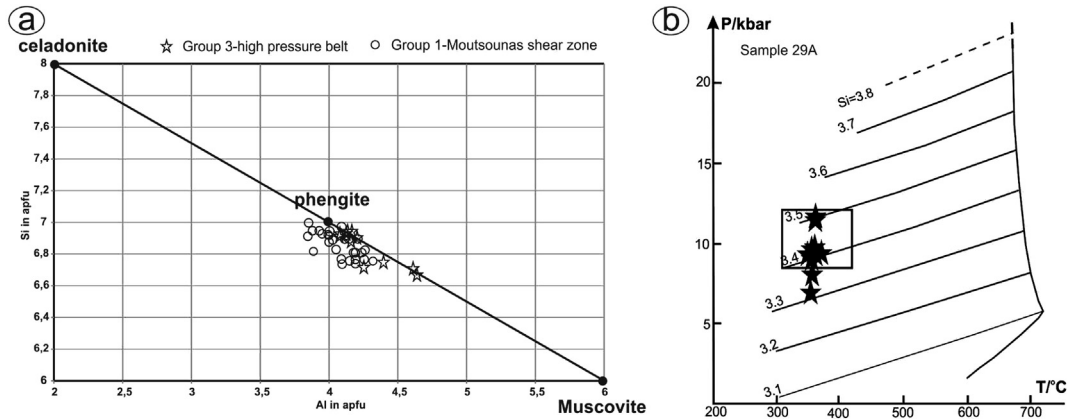
Fig. 13. (a) Classification of the representative white mica phases. Chemical analyses are summarized in Table 2. (b) Phengite geobarometry (after Massonne and Schreyer, 1987).

recrystallized grains are given in Table 4 for quartz and in Table 5 for calcite.

In quartz, the differential flow stress ranges between between 36 and 69 MPa using the equations of Twiss (1977), between 40 and 72 MPa by the method of Twiss (1980), between 29 and 54 MPa according to Stipp and Tullis (2003), and between 20 and 40 MPa using the equation of Mercier et al. (1977). In the marbles, the stress similarly ranges between 28 and 70 MPa by the Rutter (1995) piezometer and between 19 and 41 MPa using the equation of Schmid et al. (1980). The results of Ord and Christie (1984) yield a flow stress range of 40–118 MPa that seems to be too high. However, uncertainties still exist in the estimation of the flow stress from the grain size, which is influenced by the presence of other phases such as mica and chlorite, as well as the chemical environment during deformation.

8.2. Strain rate

The relationships between temperature, microstructures and CPO patterns corresponding to the dominant slip systems and thermobarometric calculations of chlorites indicate deformation under greenschist-facies conditions at temperatures of ca. 300–400 °C in the Moutsounas shear zone. We constructed deformation mechanisms of quartz aggregates at temperatures of 300, 350–400 °C. Using our flow stress and deformation temperature estimates, we calculated strain rates using the quartz flow law from the works of Hirth et al. (2001), Paterson and Luan (1990), and Koch (1983) to cover the range of available experimental results. When applied to the differential stress estimates from dynamically recrystallized grain sizes of quartz with the range covered by both
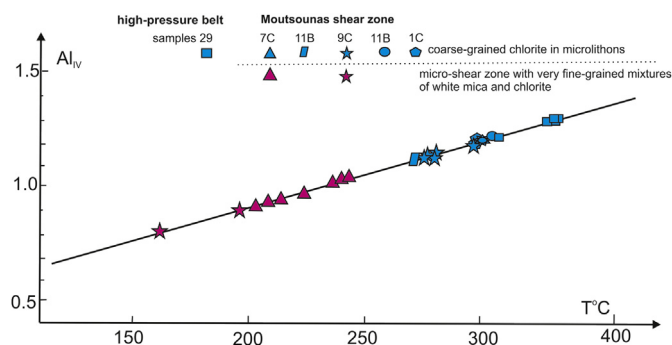
Fig. 14. Plot of parameter Al^{IV} vs. temperature for chlorite from high-pressure belt (Group 3) and Moutsounas shear zone (Group 1).

piezometers (Twiss, 1980; Stipp and Tullis, 2003), strain rate estimates from the Moutsounas shear zone range from 8.5×10^{-15}–2.3×10^{-13} S^{-1} at 300 °C, 6.1×10^{-15}–1.8×10^{-13} S^{-1} at 350 °C, and 8.1×10^{-14}–1.6×10^{-12} S^{-1} at 400 °C deformation conditions (Table 4).

The microstructures suggest that the grain size reduction of calcite was predominantly the result of subgrain rotation recrystallization accompanied by twin boundary migration suggests that mylonitization temperatures were higher than 250 °C (e.g., Burkhard, 1993; Ferrill et al., 2004; Schenk et al., 2005). Using our flow stress and deformation temperature estimates, we calculated strain rates of calcite using the flow law from the works of Walker et al. (1990) and Herwegh et al. (2005) to cover the range of available experimental results. The strain rate of calcite lies in the range of 1.1×10^{-13}–1.52×10^{-13} S^{-1} at 300 °C and 2.5×10^{-15}–2.9×10^{-15} S^{-1} at 250 °C (Walker et al., 1990) and 4.1×10^{-14} S^{-1} to 1.3×10^{-15} S^{-1} and 4.1×10^{-14}–4.9×10^{-15} S^{-1} at 250 °C (Herwegh et al., 2005) with the Rutter (1995) piezometer (Table 5).

9. Discussion

9.1. Evolution of microstructures and overprinting deformation

Microstructural analyses of the exhumed ductile Moutsounas shear zones provided insights into ductile deformation processes in the deep crust. The evolution of macro- and microstructures dominantly interpret the plastic deformation of major mineral phases (e.g. quartz, feldspar, white mica and calcite) in response to a progressive deformation history. The optical strain features including undulose extinction, planar deformation bands and subgrain formation, the development of quartz ribbons subdivided into subgrains or grains, as well as the presence of strain features in the newly recrystallized grains, indicate that dislocation creep was accompanied by dynamic recovery and dynamic recrystallization. Feldspar grains in the mylonites are occasionally characterized by irregular and serrated grain boundaries. Undulatory and inhomogeneous extinction are common in porphyroclastic feldspar grains. Dynamic recrystallization occurs in porphyroclast tails with asymmetric fabrics, which extend into layers defining the mylonitic foliation. Intense grain-size reduction of calcite generated ultramylonites. Twinning, twin migration and subgrain rotation are important processes of dynamic recrystallization of calcite in the marble mylonites within the Moutsounas shear zone. Certain rocks from the high-strain zone are completely transformed into extremely fine grains (e.g. white mica).

Table 4
Paleopiezometry data for quartz and deduced strain rates.

Sample no.	Grainsize (μm)	Differential stress (MPa)[a]					Strain rate ε̇ (1/s)[b], 300 °C			Strain rate ε̇ (1/s), 350 °C			Strain rate ε̇ (1/s), 400 °C		
	Average D	$\sigma^{(a)}$	$\sigma^{(b)}$	$\sigma^{(c)}$	$\sigma^{(d)}$	$\sigma^{(e)}$	$\dot\varepsilon^{(1)}$	$\dot\varepsilon^{(2)}$	$\dot\varepsilon^{(3)}$	$\dot\varepsilon^{(1)}$	$\dot\varepsilon^{(2)}$	$\dot\varepsilon^{(3)}$	$\dot\varepsilon^{(1)}$	$\dot\varepsilon^{(2)}$	$\dot\varepsilon^{(3)}$
1A	27	65	72	37	107	54	3.03E-15	1.89E-14	7.12E-15	2.95E-14	1.84E-13	6.79E-14	2.04E-13	1.27E-12	6.79E-14
1C	24	69	77	40	118	57	3.91E-15	2.30E-14	8.44E-15	3.80E-14	2.23E-13	8.06E-14	2.63E-13	1.55E-12	8.06E-14
7C	30	60	68	34	95	50	2.29E-15	1.52E-14	5.89E-15	2.23E-14	1.48E-13	5.62E-14	1.54E-13	1.02E-12	5.62E-14
9C	39	50	56	28	70	41	1.07E-15	8.45E-15	3.53E-15	1.04E-14	8.21E-14	3.37E-14	7.22E-14	5.69E-13	3.37E-14
11A	25	67	75	38	113	55	3.46E-15	2.10E-14	7.78E-15	3.36E-14	2.03E-13	7.43E-14	2.33E-13	1.41E-12	7.43E-14
11B	48	44	49	25	56	35	6.29E-16	5.59E-15	2.46E-15	6.11E-15	5.43E-14	2.35E-14	4.23E-14	3.76E-13	2.35E-14
28	27	65	73	37	107	54	3.07E-15	1.91E-14	7.17E-15	2.98E-14	1.85E-13	6.85E-14	2.06E-13	1.28E-12	6.85E-14
29C	33	56	62	32	83	46	1.66E-15	1.19E-14	4.74E-15	1.61E-14	1.15E-13	4.52E-14	1.12E-13	7.97E-13	4.52E-14
33B	28	62	70	36	101	52	2.63E-15	1.69E-14	6.46E-15	2.55E-14	1.64E-13	6.17E-14	1.77E-13	1.14E-12	6.17E-14
33A	64	36	40	20	40	29	2.82E-16	3.00E-15	1.43E-15	2.74E-15	2.91E-14	1.37E-14	1.90E-14	2.02E-13	1.37E-14

[a] Stress estimated using differential piezometer, $\sigma^{(a)}$ – Twiss (1977), $\sigma^{(b)}$ – Twiss (1980), $\sigma^{(c)}$ – Mercier et al. (1977), $\sigma^{(d)}$ – Ord and Christie (1984), and $\sigma^{(e)}$ – Stipp and Tullis (2003).
[b] Differential strain rate calculated based on the stress estimated by the Twiss (1980), $\dot\varepsilon^{(1)}$ strain rates calculated reference to Hirth et al., 2001, $\dot\varepsilon^{(2)}$ strain rates calculated reference to Paterson and Luan (1990), $\dot\varepsilon^{(3)}$ strain rates calculated reference to Koch (1983).

It is noteworthy that the microstructural and textural analysis has revealed the co-existence of microstructures ranging from middle-/high-temperatures to subsequent low-temperature within the Moutsounas shear zone. Quartz displays abundant evidence for early high-temperature plastic deformation (e.g. dynamic recrystallization, ribbon and polygonal grains with straight grain boundaries forming 120° triple junctions). These features suggest annealing during subsequent metamorphism and deformation at lower amphibolite facies M2 conditions (Buick, 1991a). The abundance of microstructural styles supports the later low-temperature deformational overprint during shearing. Elongated quartz ribbons, undulose and inhomogeneous extinction and deformation lamellae in quartz grains, as well as large amounts of extremely fine grains replacing ribbons, are direct evidence for low-temperature shearing. Low-temperature grain boundary migration processes or bulging recrystallization are therefore interpreted as responsible for the generation of such grains. Certain minerals such as white mica show extensive grain-size reduction in mylonites, which become ultramylonitic in some instances.

Dislocation creep, accompanied by dynamic recrystallization, was the principal deformation mechanism. Paleostress estimations of quartz and calcite suggest a flow stress within the range of 20 and 77 MPa during mylonitization. These estimates also are similar to the flow stress estimate of 28–62 MPa in quartzites, and 31–56 MPa in the marbles reported from Iraklia, a small Aegean island located to the south of Naxos (Behrmann and Seckel, 2007). Schenk et al. (2005, 2007) report very low flow stresses of ca. 2 MPa at high temperatures in marble within marbles of the migmatite dome in the center of the Naxos MCC followed by high flow stresses of 48 MPa in low-temperature (271 ± 15 °C) shear zones. Although access of hydrous fluids into the Moutsounas shear zone is documented particularly in micaschists and phyllites, water had no weakening effect in associated marbles as experiments reveal (de Bresser et al., 2005).

Based on the dynamic recrystallization grain size of quartz and the deformation temperature, we estimate that the strain rate for the mylonitic rocks of Moutsounas shear zone were 10^{-13}–10^{-15} s^{-1} for 350 °C. At high temperatures, the estimated strain rate by Schenk et al. (2007) is similar at 4×10^{-15} s^{-1}. Our strain rate estimates are in good agreement with the expected tectonic strain rates and are also similar to that of 10^{-12}–10^{-14} s^{-1} reported by Behrmann and Seckel (2007) from Iraklia island to the south of Naxos. However, the strain rate results indicate that they have no obviously different strain trend within this structural section, so more and wider testing of experimental flow laws to the well-constrained natural rocks in Naxos seems necessary.

9.2. Significance of quartz c-axes patterns

Prior to this study, the textural development of quartz in the Moutsounas shear zone was largely undocumented, although numerous high-quality data on structures and microfabrics have been published from the Naxos MCC (e.g., Buick, 1991b; Urai and Feenstra, 2001; Schenk et al., 2005, 2007; Jolivet et al., 2010; Kruckenberg et al., 2011). Quartz c-axes from the exhumed metamorphic rocks of Naxos have revealed that crystallographic preferred orientations preserve the record of polyphase deformation in these units. Asymmetric CPO patterns of quartz indicate a late top-to-the-N

Table 5
Paleopiezometry data for calcite and deduced strain rates.

Samples no.	Grainsize (μm)	[a]Differential stress (MPa)		[b]Strain rate ε̇ (1/s), 300 °C		Strain rate ε̇ (1/s), 250 °C	
	Average D	$\sigma^{(1)}$	$\sigma^{(2)}$	$\dot\varepsilon^{(1)}$	$\dot\varepsilon^{(2)}$	$\dot\varepsilon^{(1)}$	$\dot\varepsilon^{(2)}$
1D	55	45	28	1.21E-13	3.56E-15	2.68E-15	3.56E-15
7B	18	14	10	1.52E-13	4.09E-14	3.36E-15	4.09E-14
7A	87	70	41	1.11E-13	1.33E-15	2.45E-15	1.33E-15
9B	50	41	26	1.23E-13	4.26E-15	2.73E-15	4.26E-15
9C	35	28	19	1.33E-13	9.47E-15	2.94E-15	9.47E-15
7a	47	38	24	1.25E-13	4.93E-15	2.77E-15	4.93E-15
9A	50	40	25	1.24E-13	4.44E-15	2.74E-15	4.44E-15
10	52	42	26	1.23E-13	4.03E-15	2.72E-15	4.03E-15
7B	48	39	25	1.24E-13	4.65E-15	2.75E-15	4.65E-15
11C	54	44	27	1.22E-13	3.66E-15	2.69E-15	3.66E-15

[a] Stress estimated using differential piezometer, $\sigma^{(1)}$ - Rutter (1995), $\sigma^{(2)}$ - Schmid et al. (1980).
[b] Differential strain rate (ε̇) calculated based on the stress estimated by the Rutter (1995), $\dot\varepsilon^{(1)}$ strain rates calculated reference to Walker et al. (1990), $\dot\varepsilon^{(2)}$ strain rates calculated reference to Herwegh et al. (2005).

or NNE shear, which is consistent with field and microstructure observations. The activation of slip systems of quartz is temperature-sensitive because the *c*-axis orientation of quartz changes with temperatures (e.g., Stipp et al., 2002; Passchier and Trouw, 2005). Prism <a> slip is commonly observed in high-grade metamorphic rocks (e.g., Egydio-Silva et al., 2002; Otani and Wallis, 2006) and the basal <a> slip is observed in low-grade or overprinted metamorphic rocks (e.g. Toy et al., 2008; Cao et al., 2010, 2011a, b). Quartz from the granitic gneisses and quartz-rich mylonites in the Naxos MCC exhibits numerous slip systems, including high-temperature slip systems: combined prisms <a> and rhomb<a> and low-temperature basal <a> slip. The development of strong quartz textures close to the migmatite dome and in the southern high-pressure belt of the Naxos MCC indicates high-middle temperature at amphibolite facies metamorphic conditions. High-temperature conditions were likely sufficient to influence deformation at higher structural levels, thereby facilitating localization of ductile strain. Medium-temperature shearing is responsible for the generation of the point maxima, which are characterized by ribbon quartz grains or grain aggregates. Low-temperature shearing is evidenced by muscovite grain size reduction and the formation of mica fish, and is also reflected in the quartz microfabrics.

Quartz *c*-axis fabric open-angles have been proposed as a potential thermometer by Kruhl (1996) with opening angles increasing as the component of prism <c> and prism <a> slip becomes more important with increasing deformation temperatures. The Y point maxima (Group 2) suggests deformation-induced grain boundary migration recrystallization under high- or medium-temperature conditions from 300 °C to 600 °C (e.g. Stipp et al., 2002), which is consistent with optical observations. These texture patterns imply that the high-temperature deformation is mostly preserved in the migmatite dome and high-pressure belt and locally in the eastern Moutsounas shear zone. It is also noteworthy that these fabrics are formed by Y maxima superimposition onto crossed girdles or a single girdle. The superimposition is well supported by microstructural studies, which reveal that most sheared rocks from the high-pressure belt and the Moutsounas shear zone are relics of early high-temperature deformation. The high-temperature microstructures and textures are partly or entirely transposed by subsequent late low-temperature shearing. Therefore, the high-temperature conditions should be the results of an early event (M1 or peak conditions of M2). As suggested by Toy et al. (2008), the strong Y-maxima of quartz from the mylonites and ultramylonites result from high ductile shear strains under amphibolite facies conditions deep within the crust. The development of these strong fabrics represents combined prism <a> and rhomb <a> slip. During exhumation, basal <a> slip is likely to become the more favored system, but the inherited strong high-temperature fabrics mean that prism <a> slip is likely to continue in these strongly oriented rocks. Basal <a> slip is dominant at lower temperature simple shear and at faster strain rates, causing a *c*-axis fabric maximum near the Z-axis of the finite strain ellipsoid.

9.3. Significance of calcite textures

Plastic deformation of calcite occurs in low- and high-temperature regimes (e.g. Wenk et al., 1987; Leiss and Barber, 1999; Pieri et al., 2001a, b; Liu et al., 2002; Leiss and Molli, 2003; Bestmann et al., 2000; Romeo et al., 2007). The marble mylonites from the Moutsounas shear zone present different calcite texture types, which are related to meso- and microstructures and textures. Deformation accommodated twin and grain boundary migration, subgrain rotation, e-twinning slip and intra-crystalline slip observed in the microstructures are important processes of dynamic recrystallization, and suggest that the texture patterns are probably influenced by dynamic recrystallization. These

observations suggest that calcite crystals were deformed by intra-crystalline plastic deformation (dislocation creep and twinning), which was accommodated by dissolution-precipitation. A progressive development of c-axes of calcites from the ultramylonites, mylonites and mylonitic calc-schist is well exhibited. The occurrence of the c-axis and e-pole great circle girdle textures normal to lineation appears to be produced in the initial stages of deformation. Subsequent progressive deformation rapidly gives way to other mechanisms, with strain increments giving rise to different LPOs (the c-maximum normal to lineation) and markedly changing the main shape fabric. At a low strain, the observed crystal flow behavior is best characterized by deformation through grain boundary sliding associated with dislocation creep processes, and dynamic recrystallization by subgrain rotation and grain bulging dominates (e.g. Schmid et al., 1977; Walker et al., 1990; Romeo et al., 2007). On the other hand, in coarse-grained rocks, deformation is associated with dislocation creep processes and dynamic recrystallization by grain boundary migration (Schmid et al., 1980; Rutter, 1995). Fabric softening (i.e. LPO) leads to crystal alignment in easy slip orientations (e.g., Poirier, 1980; Rutter et al., 1994, 1998; Pieri et al., 2001a, b). These CPO patterns suggest that high-temperature deformation is controlled by slip on {0001} <11−20> (c<a>) and a low-temperature deformation is characterized by twinning on {−1018}<11−20>(e<a>). The (c<a>) and e<a> could have been active during deformation. However, c<a> is possibly the dominant slip system deformation at high shear strain dynamic recrystallization, because the {c} maximum is stronger than the {e} one in the Z-axes normal to the shear foliation. In this case, the texture of calcite was controlled by c<a>, combined with a low-temperature slip e<a>, which can be interpreted as the texture developed during exhumation. The different textures in the mylonite and ultramylonites also suggest a different amount of shear strain in which the concentration of deformation could have played a role. The amount of dynamic recrystallization increases with strain (e.g., Pieri et al., 2001b; Barnhoorn et al., 2004). The different rocks (e.g., mylonites and ultramylonites) experienced different strains under different strain regimes, which resulted from contrasting rheological behavior during deformation. The wider maxima of CPOs (e.g. samples 7A, 10C) could be related to a certain degree of thermal annealing after deformation as suggested by Barnhoorn et al. (2005). The asymmetry of the c-axis point maximum with respect to the shear plane has also been observed in porphyroclasts and recrystallized grains (e.g. sample 7A), indicating a sinistral sense of shear in agreement with the general kinematics of the shear zone.

Microfabrics and patterns of textures in calcite mylonites are sensitive to final stages of deformation (e.g. Lister and Williams, 1979). Therefore, the microfabrics and texture patterns of calcite can here document the kinematic character during the late, low-temperature stage of exhumation. It seems probable that the marbles have undergone a component of early coaxial deformation during the exhumation of the MCC. Simple shear is recorded in the mylonites and locally in ultramylonites. Compared to plastically deformed marble mylonites, non-coaxial deformation components on the calc-schists cannot be completely ruled out, but their effects are not obvious. Strain concentration during extension under retrograde conditions resulted in the localization of deformation in a narrow zone (Bestmann et al., 2000), where the imposed bulk strain is partitioned into simultaneously deforming coaxial and non-coaxial zones and pervasive dynamic recrystallization occurred in the shear zone.

9.4. Timing of the Moutsounas shear zone

No detailed petrological P-T data and only a few geochronological mineral ages are available from the Moutsounas shear zone ss mentioned earlier. Along the Moutsounas shear zone, the M2

temperature should diminish southward and the Eocene M1 meta-morphism should dominate. Consequently, the temperature before retrogression after M1 and M2 metamorphism is similar along the strike of the Moutsounas shear zone. The following geochronological mineral ages are known from the Moutsounas shear zone. Andriessen et al. (1979, 1991) reported four K–Ar white mica ages including 37.9 ± 0.9, 36.8 ± 1.1, 32.2 ± 0.9 and 41.8 ± 1.3 Ma from the southern portion of the Moutsounas shear zone $^{40}Ar/^{39}Ar$ phengite ages for the M1 metamorphism were dated at 45 ± 5 Ma by Wijbrans and McDougall (1986, 1988). Seward et al. (2009) report a zircon fission track age of 10.6 ± 1.2 Ma for the Moutsounas locality.

Consequently, no accurate age can be given for shearing. The minimum age must be at the younger age limit of the range of 19 to 14 Ma for M2 metamorphism (Keay, 1998; Keay et al., 2001; Martin et al., 2006) and older than the zircon fission track age of 10.6 ± 1.2 Ma (Seward et al., 2009). These constraints make it likely that the normal faulting largely postdates the metamorphism M1, is constrained between ca. 14 and 10.6 Ma and occurred late during the deposition of the Pesulia Formation and is contemporaneous with initial stages of the Eromonisia Formation. However, a potential problem exists concerning the more precise chronostratigraphic in-dicators to limit its minimum timing of crystal fabric development relative to plastic deformation and dynamic recrystallization. Therefore, the time of shearing should be dated by future $^{40}Ar/^{39}Ar$ dating of single white grains grown during shearing.

The above mentioned large range of ages for the transition from M1 to M2 is explained by two models: (1) Buick and Holland (1989) invoked a progressive temperature increase during exhumation on the basis of thermobarometric data obtained on samples from different parts of the island. (2) Wijbrans and McDougall (1988) argued for partial thermal resetting of the HP–LT M1 paragenesis after its exhumation.

9.5. Stability of white mica and chlorite in sheared rocks

The new data from fine-grained sheared rocks reveal that earlier formed phengite-rich white mica potentially remains stable although later mechanical overprint during shearing. In contrast, chlorite is found to loose stability even within subgreenschist facies metamorphic conditions during shearing. A reason could be the interaction of older mineral assemblages with hydrous fluids, possibly hydrothermal fluids along the shear zone. This is believed to reset the chemical composition of chlorite. The final tempera-tures of chlorite thermometry need independent proof by other methods (e.g. de Caritat et al., 1993). We are taking, therefore, the temperatures of the chlorite thermometry only as approximate preliminary values. However, the data show that earlier micro-fabrics as those in microlithons (Type 1) yield higher temperatures than the subsequent sheared chlorites (Type 2). If the temperatures are approximately correct this would suggest that ductile shear in phyllosilicate-rich rocks could potentially occur at subgreenschist facies metamorphic conditions.

9.6. Tectonic interpretation of the Moutsounas shear zone

Since the discovery of the MCC of the lower unit at Naxos, the shear zone at the eastern boundary was considered as a normal fault toward the east (e.g. Lister et al., 1984; Gautier et al., 1993; Jolivet et al., 1994) because of the juxtaposition of metamorphic rocks toward unmetamorphosed uppermost Oligocene to Miocene sediments (see also Vanderhaeghe et al., 2007). We consider the Moutsounas shear zone as a ductile oblique-slip low-angle normal fault with a motion of the hangingwall units toward the NNE. Later, the ductile oblique-slip fault was steepened due to subsequent E–W shortening. The E–W shortening is a late-stage process, which

also resulted in the updoming of the MCC (Kruckenberg et al., 2011 and references therein) and in the formation of a synclinal structure containing Miocene sediments between the MCC in the east and the Naxos granodiorite in the west (Fig. 3b). The structures along the eastern upper margin of the Moutsounas shear zone strongly correlate to contemporaneous structures like NNE shear and E-W shortening by folding (Urai et al., 1990; Vanderhaeghe, 2004; Kruckenberg et al., 2011) within the interior of the Naxos MCC.

10. Conclusions

(1) We interpret the east-dipping Moutsounas shear zone as a lateral boundary of the Naxos MCC, which bounds tilted Miocene sediments exposed in the eastern hangingwall unit. Microstructural and textural analysis of samples and field ob-servations reveals that the movement along the Moutsounas shear zone is associated with retrograde metamorphism, in which greenschist- and sub-greenschist metamorphic condi-tions overprinted the early high-temperature rocks (lower amphibolite facies).

(2) The Moutsounas shear zone formed in response to regional extension of Aegean continental crust. Extension on Naxos was accommodated, in part, by top-to-the-NNE ductile to ductile-brittle simple shear within greenschist-facies conditions. The microstructures and c-axis fabrics, taken together, disclose that ductile and brittle deformation was achieved by penetrative, non-coaxial deformation dominated by progressive simple shear.

(3) Based on the microstructure, texture and grain size of recrys-tallized quartz and calcite, we estimate that the differential stress and strain rate for the mylonitic rocks were respectively 20–77 MPa and 10^{-15}–10^{-13} s^{-1} ca. 350 °C for quartz and ca. 300 °C for calcite.

(4) Combined with published geochronological data, microstruc-tures of samples and field observations, this indicates that the Moutsounas shear zone of the Naxos MCC is related to the main activity with a top-to-the-NNE shear with the main stage of updoming during migmatite formation and associated exhu-mation between ca. 15 and 11 Ma.

(5) Chlorite thermometry of the Moutsounas shear zone reveals two temperature groups, 300–360 °C, and 200–250 °C, are related to late stages of shearing. The lower temperature group is interpreted to result from late-stage hydrothermal overprint, which affected also older chlorite-bearing microfabrics. Chlo-rite in sheared rocks is likely accessible to late-stage resetting.

References

Altherr, R., Kreuzer, H., Wendt, I., Lenz, H., Wagner, G.A., Keller, J., Harre, W., Hohndorf, A., 1982. A late oligocene/early miocene high temperature belt in the Attic-Cycladic crystalline complex (SE Pelagonian, Greece). Geologisches Jahr-buch 23, 97–164.
Andriessen, P.A.M., 1991. K-Ar and Rb-Sr age determinations on micas of impure marbles of Naxos, Greece: the influence of metamorphic fluids and lithology on the blocking temperature. Schweizerische Mineralogische und Petrographische Mitteilungen 71, 89–99.

Andriessen, P.A.M., Banga, G., Hebeda, E.H., 1987. Isotopic age study of pre-Alpine rocks in the basal units on Naxos, Sikinos and Ios, Greek Cyclades. Geologie en Mijnbouw 66, 3–14.

Andriessen, P.A.M., Boelrijk, N.A.I.M., Hebeda, E.H., Priem, H.N.A., Verdurmen, E.A.T., Verschure, R.H., 1979. Dating the events of metamorphism and granitic magmatism in the Alpine Orogen of Naxos (Cyclades Greece). Contributions to Mineralogy and Petrology 69, 215–225.

Angelier, J., Glacon, G., Müller, C., 1978. Sur l'existance et la position tectonique du Miocène inférieur marin des l'archipel de Naxos (Cyclades, Grèce). Comptes Rendus Academie de Société de Paris 286, 21–24.

Angelier, J., Lyberis, N., Le Pichon, X., Barrier, E., Huchon, P., 1982. The tectonic development of the Hellenic arc and the Sea of Crete: a synthesis. Tectonophysics 86, 159–196.

Austin, N.J., Evans, B., 2007. Paleowattmeters: a scaling relation for dynamically recrystallized grain size. Geology 35, 343–346. http://dx.doi.org/10.1130/G23244A.1.

Avigad, D., 1998. High-pressure metamorphism and cooling on SE Naxos (Cyclades, Greece). European Journal of Mineralogy 10, 1309–1319.

Avigad, D., Garfunkel, Z., 1991. Uplift and exhumation of high-pressure metamorphic terrains: the example of the Cycladic blueschist belt (Aegean Sea). Tectonophysics 188, 357–372.

Bargnesi, E.A., Stockli, D., Mancktelow, N., Soukis, M., 2012. Miocene core complex development and coeval supradetachment basin evolution of Paros, Greece, insights from (U–Th)/He thermochronometry. Tectonophysics 595–596, 165–182.

Barnhoorn, A., Bystricky, M., Burlini, L., Kunze, K., 2004. The role of recrystallization on the deformation behaviour of calcite rocks: larg strin torsion experiments on Carrara marble. Journal of Structural Geology 26, 885–903.

Barnhoorn, A., Bystricky, M., Burlini, L., Kunze, K., 2005. Post-deformational annealing of calcite rocks. Tectonophysics 403, 167–191.

Behrmann, J., 1985. Crystal plasticity and superplasticity in quartzite-a natural example. Tectonophysics 115, 101–129.

Behrmann, J.H., Seckel, C., 2007. Structures, flow stresses, and estimated strain rates in metamorphic rocks of the Small Cyclades Islands Iraklia and Schinoussa (Aegean Sea, Greece). Geotectonic Research 95, 1–11.

Bestmann, M., Kunze, K., Matthews, A., 2000. Evolution of a calcite marble shear zone complex on Thassos Island, Greece: microstructural and textural fabrics and their kinematic significance. Journal of Structural Geology 22, 1789–1807.

Böger, H., 1983. Stratigraphische und tektonische Verknuepfungen kontinentaler Sedimente des Neogens im Aegais-Raum. Geologische Rundschau 72, 771–813.

Bohnhoff, M., Rische, M., Meier, T., Endrun, B., Harjes, H.-P., Stavrakakis, G., 2004. A temporary seismic network on the Cyclades (Aegean Sea, Greece). Seismological Research Letters 75, 352–357.

Boronkay, K., Doutsos, T., 1994. Transpression and transtension within different structural levels in the central Aegean region. Journal of Structural Geology 16, 1555–1573.

Brichau, S., Ring, U., Ketcham, R.A., Carter, A., 2006. Constraining the long–term evolution of the slip rate for a major extensional fault system in the central Aegean, Greece, using thermochronology. Earth and Planetary Science Letters 241, 293–306.

Brichau, S., Thomson, S., Ring, U., 2010. Thermochronometric constraints on the tectonic evolution of the Serifos detachment, Aegean Sea, Greece. International Journal of Earth Sciences 99, 379–393.

Brun, J.P., Sokoutis, D., 2007. Kinematics of the southern Rhodope core complex (North Greece). International Journal of Earth Sciences (Geol Rundsch) 96, 1079–1099.

Brunel, M., 1980. Quartz fabrics in shear zones mylonites: evidence of a major imprint due to late strain increments. Tectonophysics 64, 33–44.

Buick, I.S., 1991a. The late Alpine evolution of an extensional shear zone, Naxos, Greece. Journal of the Geological Society of London 148, 93–103.

Buick, I.S., 1991b. Mylonite fabric development on Naxos, Greece. Journal of Structural Geology 13, 643–655. http://dx.doi.org/10.1016/0191-8141(91)90027-G.

Buick, I.S., Holland, T.J.B., 1989. The P–T–t path associated with crustal extension, in Evolution of Metamorphic Belts. In: Geological Society London, Special Publications, vol. 43, pp. 365–369.

Burkhard, M., 1993. Calcite twins, their geometry, appearance and significance as stress-strain markers and indicators of tectonic regime: a review. Journal of Structural Geology 15, 351–368.

Cao, S.Y., Liu, J.L., Hu, L., 2010. Orientation-related deformation mechanisms of naturally deformed amphibole in amphibolite mylonites from the Diancang Shan, SW Yunnan, China. Journal of Structural Geology 32, 606–622.

Cao, S.Y., Neubauer, F., Liu, J.L., Genser, J., Leiss, B., 2011a. Exhumation of the Diancang Shan metamorphic complex along the Ailao Shan-Red River belt, Yunnan, southwestern, China: evidence from $^{40}Ar/^{39}Ar$ thermochronology. Journal of Asian Earth Science 42, 525–550.

Cao, S.Y., Liu, J.L., Leiss, B., Vollbrecht, A., Genser, J., Neubauer, F., Zhao, C.Q., 2011b. Initiation of left-lateral deformation along the Ailao Shan-Red River shear zone: new microstructural, textural and geochronological constraints from the Diancang Shan metamorphic massif, SW Yunnan, China. International Geology Review 54, 348–367. http://dx.doi.org/10.1080/00206814.2010.543789.

Cathelineau, M., 1988. Cation site occupancy in chlorites and illites as a function of temperature. Clay Minerals 23, 471–485.

Cathelineau, M., Nieva, D., 1985. A chlorite solid solution geothermometer. The Los Azufres (Mexico) geothermal system. Contributions to Mineralogy and Petrology 91, 235–244.

Coney, P., 1987. The regional tectonic setting and possible causes of Cenozoic extension in the North American Cordillera. In: Geological Society London, Special Publications, vol. 28, pp. 177–186.

Coney, P., Harms, T., 1984. Cordilleran metamorphic core complexes: Cenozoic extensional relics of Mesozoic compression. Geology 12, 550–554.

Davis, G.H., 1983. Shear-zone model for the origin of metamorphic core complexes. Geology 11, 342–347.

de Bresser, J., Ter Heege, J., Spiers, C., 2001. Grain size reduction by dynamic recrystallization: can it result in major rheological weakening? International Journal of Earth Science 90, 28–45.

de Bresser, J.H.P., Urai, J.L., Olgaard, D.L., 2005. Effect of water on the strength and microstructure of Carrara marble axially deformed at high temperatures. Journal of Structural Geology 27 (2), 265–281.

de Caritat, P., Hutcheon, I., Walshe, J.L., 1993. Chlorite geothermometry: a review. Clays and Clay Minerals 41, 219–239.

Duchêne, S., Aissa, R., Vanderhaeghe, O., 2006. Pressure-temperature-time evolution of metamorphic rocks from Naxos (Cyclades, Greece): constraints from thermobarometry and Rb/Sr dating. Geodinamica Acta 19, 301–321.

Doutsos, T., Kokkalas, S., 2001. Stress and deformation patterns in the Aegean region. Journal of Structural Geology 23, 455–472.

Egydio-Silva, M., Vauchez, A., Bascou, J., Hippertt, J., 2002. High-temperature deformation in the Neoproterozoic transpressional Ribeira belt, southeast Brazil. Tectonophysics 352, 203–224.

Ferrill, D.A., Morris, A.P., Evans, M.A., Burkhard, M., Groshong, R.H., Onasch, C.M., 2004. Calcite twin morphology: a low-temperature deformation geothermometer. Journal of Structural Geology 26, 1521–1529. http://dx.doi.org/10.1016/j.jsg.2003.11.028.

Floyd, M.A., Billiris, H., Paradissis, D., Veis, G., Avallone, A., Briole, P., McClusky, S., Nocquet, J.M., Palamartchouk, K., Parsons, B., 2010. A new velocity field for Greece: implications for the kinematics and dynamics of the Aegean. Journal of Geophysical Research 115, B10403. http://dx.doi.org/10.1029/2009JB007040.

Gautier, P., Ballévre, M., Brun, J.P., Jolivet, L., 1990. Extension ductile et bassins sédimentaires mio-liocénes dans les Cyclades (îles de Naxos et Paros). In: Comptes Rendus de l'Académie des Sciences. Série I. Mathématique, vol. 310, pp. 147–153.

Gautier, P., Brun, J.P., Jolivet, L., 1993. Structure and kinematics of upper Cenozoic extensional detachment on Naxos and Paros (Cyclades Islands, Greece). Tectonics 12, 1180–1194.

Grasemann, B., Schneider, D.A., Stöckli, D.F., Iglseder, C., 2012. Miocene bivergent crustal extension in the Aegean: evidence from the western Cyclades (Greece). Lithosphere 4, 23–29.

Gueydan, F., Mehl, C., Parra, T., 2005. Stress-strain rate history of a midcrustal shear zone and the onset of brittle deformation inferred from quartz recrystallized grain size. In: Geological Society London, Special Publications, vol. 243, pp. 127–142. http://dx.doi.org/10.1144/GSL.SP.2005.243.01.10.

Hacker, B.R., Yin, A., Christie, J.M., Davis, G.A., 1992. Stress magnitude, strain rate, and rheology of extended middle continental crust inferred from quartz grain sizes in the Whipple Mountains, California. Tectonics 11, 36–46. http://dx.doi.org/10.1029/91TC01291.

Hatzfeld, D., Besnard, M., Makropoulos, K., Voulgaris, N., Kouskouna, V., Hatzidimitriou, P., Panagiotopoulos, D., Karakaisis, G., Deschamps, A., Lyon-Caen, H., 1993. Subcrustal microearthquake seismicity and fault plane solutions beneath the Hellenic Arc. Journal of Geophysical Research 98, 9861–9870.

Hejl, E., Riedl, H., Soulakellis, N., Van De Haute, P., Weingartener, H., 2003. Young Neogene tectonics ad relief development on the Aegean islands of Naxos, Paros and Ios (Cyclades, Greece). Mitteilungen Österreichischen Geologischen Gesellschaft 93, 105–127.

Hejl, E., Riedl, H., Weingartner, H., 2002. Post-plutonic unroofing and morphogenesis of the Attic-Cycladic complex (Aegea, Greece). Tectonophysics 349, 37–56.

Henjes-Kunst, F., Altherr, R., Kreuzer, H., Hansen, B.T., 1988. Disturbed U-Th-Pb systematics of young zircons and uranothorites: the case of the Miocene Aegean granitoids (Greece). Chemical Geology 73, 125–145.

Herwegh, M., de Bresser, J.H.P., ter Heege, J.H., 2005. Combining natural microstructures with composite flow laws: an improved approach for the extrapolation of lab data to nature. Journal of Structural Geology 27, 503–521.

Herwegh, M., Kunze, K., 2002. The influence of nano-scale second-phase particles on deformation of fine grained calcite mylonites. Journal of Structural Geology 24, 1463–1478.

Hirth, G., Teyssier, C., Dunlap, W.J., 2001. An evaluation of quartzite flow laws based on comparisons between experimentally and naturally deformed rocks. International Journal of Earth Science 90, 77–87.

Hirth, G., Tullis, J., 1992. Dislocation creep regimes in quartz aggregates. Journal of Structural Geology 14, 145–159.

Huet, B., Pourhiet, L.L., Labrousse, L., Burov, E.B., Jolivet, L., 2011. Formation of metamorphic core complex in inherited wedges: a thermomechanical modelling study. Earth and Planetary Science Letters 309, 249–257.

Hollenstein, C.M., Müller, M.D., Geiger, A., Kahle, H.G., 2008. Crustal motion and deformation in Greece from a decade of GPS measurements, 1993–2003. Tectonophysics 449, 17–40.

Jacobshagen, V., 1986. Geologie von Griechenland. Berlin (Gebrüder Borntraeger), p. 636.

Jansen, J.B.H., 1973. Geological Map of Naxos-Nation. Inst. of Geology and Mining Research, Athens.

Jansen, J.B.H., 1977. The geology of Naxos. Geology and Geophysical Research [Athens, Greece] 19, 1–100.

Jansen, J.B.H., Schuiling, R.D., 1976. Metamorphism on Naxos: petrology and geothermal gradients. American Journal of Science 276, 1225–1253.

John, B.E., Howard, K.A., 1995. Rapid extension recorded by cooling-age patterns and brittle deformation, Naxos, Greece. Journal of Geophysical Research, 9969–9979.

Jolivet, L., Famin, V., Mehl, C., Parra, T., Aubourg, C., Hébert, R., Philippot, P., 2004. Strain localization during crustal–scale boudinage to form extensional metamorphic domes in the Aegean Sea, In: Gneiss Domes in Orogeny. Geological Society of America 380, 185–210.

Jolivet, L., Faccenna, C., Piromallo, C., 2009. From Mantle to crust: stretching the Mediterranean. Earth and Planetary Science Letter 285, 198–209. http://dx.doi.org/10.1016/j.epsl.2009.06.017.

Jolivet, L., Lecomte, E., Huet, B., Denèle, Y., Lacombe, O., Labrousse, L., Le Pourhiet, L., Mehl, C., 2010. The north Cycladic detachment system. Earth and Planetary Science Letters 289, 87–104.

Jolivet, L., Brun, J.-P., Gautier, P., Lallemant, S., Patriat, M., 1994. 3Dkinematics of extension in the Aegean region from the early Miocene to the present: insights from the ductile crust. Bulletin de la Société Géologique Geologique de France 165 (3), 195–209.

Jolivet, L., Patriat, M., 1999. Ductile extension and the formation of the Aegean Sea. In: Durand, B., Jolivet, L., Horvàth, F., Séranne, M. (Eds.), The Mediterranean Basins: Tertiary Extension within the Alpine Orogen, Geological Society Special Publication. Geological Society London, vol. 156, pp. 427–456.

Jowett, E.C., 1991. Fitting iron and magnesium into the hydrothermal chlorite geothermometer. In: GAC/MAC/SEG Joint Annual Meeting (Toronto, May 27.29, 1991). Program with Abstracts 16, A62. Toronto.

Keay, S., 1998. The Geological Evolution of the Cyclades, Greece: Constraints from SHRIMP U-Pb Geochronology. PhD thesis. Australian National University, Canberra, p. 341.

Keay, S., Lister, G., Buick, I., 2001. The timing of partial melting, Barrovianmetamorphism and granite intrusion in the Naxosmetamorphic core complex, Cyclades, Aegean Sea, Greece. Tectonophysics 342, 275–312. http://dx.doi.org/10.1016/S0040-1951(01)00168-8.

Koch, P., 1983. Rheology and Microstructures of Experimentally Deformed Quartz Aggregates. Ph.D. thesis. University of California, Los Angeles.

Koukouvelas, I.K., Kokkalas, S., 2003. Emplacement of the Miocene west Naxos pluton (Aegean sea, Greece): a structural study. Geological Magazine 140, 45–61.

Krabbendam, M., Urai, J.J., Vliet, L.J., 2003. Grain size stabilisation by dispersed graphite in a high-grade quartz mylonite: an example from Naxos (Greece). Journal of Structural Geology 25, 855–866.

Kranidiotis, P., MacLean, W.H., 1987. Systematics of chlorite alteration at the Phelps Dodge massive sulfide deposit, Matagami, Quebec. Economic Geology 82, 1898–1911.

Kruckenberg, S.C., Ferré, E.C., Teyssier, C., Vanderhaeghe, O., Whitney, D.L., Seaton, N.C.A., Skord, J.A., 2010. Viscoplastic flow in migmatites deduced from fabric anisotropy: an example from the Naxos dome, Greece. Journal of Geophysical Research 115, B09401.

Kruckenberg, S.C., Vanderhaeghe, O., Ferré, E.C., Teyssier, C., Whitney, D.L., 2011. Flow of partially molten crust and the internal dynamics of a migmatite dome, Naxos, Greece. Tectonics 30, TC3001. http://dx.doi.org/10.1029/2010TC002751.

Kruhl, J.H., 1996. Prism- and basal-plane parallel subgrain boundaries in quartz: a microstructural geothermobarometer. Journal of Metamorphic Geology 14, 581–589.

Kuhlemann, J., Frisch, W., Dunkl, I., Kázmér, M., Schmiedl, G., 2004. Miocene siliciclastic deposits of Naxos Island: geodynamic and environmental implications for the evolution of the southern Aegean Sea (Greece). In: Geological Society of America, Special Paper, vol. 378, pp. 51–65.

Law, R.D., 1986. Relationships between strain and quartz crystallographic fabrics in the Roche Maurice Quartzites of Plougastel, western Brittany. Journal of Structural Geology 8, 493–516.

Lee, J., Lister, G.S., 1992. Late Miocene ductile extension and detachment faulting, Mykonos, Greece. Geology 20, 121–124.

Leiss, B., Molli, G., 2003. "High-Temperature" texture in naturally deformed Carrara marble from the Alpi Apuane, Italy. Journal of Structural Geology 25, 649–658.

Leiss, B., Barber, D.J., 1999. Mechanisms of dynamic recrystallization in naturally deformed dolomite inferred from EBSP-analyses. Tectonophysics 303, 51–69.

Lewis, S., Holness, M., Graham, C., 1998. Ion microprobe study of marble from Naxos, Greece: Grain-scale fluid pathways and stable isotope equilibration during metamorphism. Geology 26, 935–938.

Le Pichon, X., Angelier, J., 1979. The Hellenic Arc and Trench system: a key to the Neotectonic evolution of the eastern Mediterranean area. Tectonophysics 60, 1–42.

Lister, G.S., Banga, C., Feenstra, A., 1984. Metamorphic core complexes of Cordilleran type in the Cyclades, Aegean Sea, Greece. Geology 12, 221–225.

Lister, G.S., Davis, G.A., 1989. The origin of metamorphic core complexes and detachment faults formed during Tertiary continental extension in the northern Colorado River region, U.S.A. Journal of Structural Geology 11, 65–94.

Lister, G.S., Snoke, A.W., 1984. S-C mylonites. Journal of Structural Geology 6, 617–638.

Lister, G.S., Williams, P.F., 1979. Fabric development in shear zones: theoretical controls and observed phenomena. Journal of Structural Geology 1, 283–297.

Liu, J.L., Walter, J.M., Weber, K., 2002. Fluid-enhanced low-temperature plasticity of calcite marble: microstructures and mechanisms. Geology 30, 787–790.

Liu, J.L., Tang, Y., Tran, M.-D., Cao, S.Y., Zhao, Z.C., Zhao, Z.D., Chen, W., 2012. The nature of the Ailao Shan–Red River (ASRR) shear zone: constraints from structural, microstructural and fabric analyses of metamorphic rocks from the Diancang Shan, Ailao Shan and Day Nui Con Voi massifs. Journal of Asian Earth Sciences 47, 231–251.

Martin, L.A.J., Duchêne, S., Deloule, E., Vanderhaeghe, O., 2008. Mobility of trace elements and oxygen in zircon during metamorphism: Consequences for geochemical tracing. Earth and Planetary Science Letters 267, 161–174. http://dx.doi.org/10.1016/j.epsl.2007.11.029.

Martin, L., Duchêne, S., Deloule, E., Vanderhaeghe, O., 2006. The isotopic composition of zircon and garnet: a record of the metamorphic history of Naxos, Greece. Lithos 87, 174–192.

Massonne, H.J., Schreyer, W., 1987. Phengite geobarometry based on the limiting assemblage with K-feldspar, phlogopite, and quartz. Contributions to Mineralogy and Petrology 96, 212–224.

Massonne, H.J., Szpurka, Z., 1997. Thermodynamic properties of white micas on the basis of high pressure experiments in the systems $K_2O–MgO–Al_2O_3–SiO_2$ and $K_2O–FeO–Al_2O_3–SiO_2–H_2O$. Lithos 41, 229–250.

McClusky, S., Balassanian, S., Barka, A., Demir, C., Ergintav, S., et al., 2000. Global Positioning System constraints on plate kinematics and dynamics in the eastern Mediterranean and Caucasus. Journal of Geophysical Research 105, 5695–5719.

Mehl, L., Hirth, G., 2008. Plagioclase preferred orientation in layered mylonites: evaluation of flow laws for the lower crust. Journal of Geophysical Research 113, B05202. http://dx.doi.org/10.1029/2007JB005075.

Mercier, J.C.C., Anderson, D.A., Carter, N.L., 1977. Stress in the lithosphere: Inferences from steady-state flow of rocks. Pure and Applied Geophysics 115, 199–226.

Okrusch, M., Bröcker, M., 1990. Eclogites associated with high-grade blueschist in the Cyclades archipelago, Greece: a review. European Journal of Mineralogy 2, 451–476.

Okudaira, T., Shigematsu, N., 2012. Estimates of stress and strain rate in mylonites based on the boundary between the fields of grain-size sensitive and insensitive creep. Journal of Geophysical Research 117, B03210. http://dx.doi.org/10.1029/2011JB008799.

Ord, A., Christie, J.M., 1984. Flow stresses from microstructures in mylonitic quartzites of the Moine thrust zone, Assynt area, Scotland. Journal of Structural Geology 6, 639–654.

Otani, M., Wallis, S.R., 2006. Quartz lattice preferred orientation patterns and static recrystallization: natural examples from the Ryoke belt, Japan. Geology 34, 561–564.

Passchier, C.W., Trouw, R.A.J., 2005. Microtectonics. Springer-Verlag, Berlin, p. 366.

Paterson, M.S., Luan, F.C., 1990. Quartzite rheology under geological conditions. In: Knipe, R.J., Rutter, E.H. (Eds.), Deformation Mechanisms, Rheology and Tectonics, Geological Society London Special Publication, vol. 54, pp. 299–307.

Pe-Piper, G., 2000. Origin of S-type granites coeval with I-type granites in the Hellenic subduction system, Miocene of Naxos, Greece. European Journal of Mineralogy 12, 859–875.

Pe-Piper, G., Kotopouli, C.N., Piper, D.J.W., 1997. Granitoid rocks of Naxos, Greece; regional geology and petrology. Geological Journal 32, 153–171.

Pieri, M., Burlini, L., Kunze, K., Stretton, I., Olgaard, D.L., 2001a. Rheological and microstructural evolution of Carrara marble with high shear strain: results from high temperature torsion experiments. Journal of Structural Geology 23, 1393–1413.

Pieri, M., Kunze, K., Burlini, L., Stretton, I., Olgaard, D.L., Burg, J.P., Wenk, H.R., 2001b. Texture development of calcite by deformation and dynamic recrystallisation at 1000 K during torsion experiments of marble to large strains. Tectonophysics 330, 119–140.

Poirier, P., 1980. Shear localization and shear in stability in materials in the ductile field. Journal of Structural Geology 2, 135–142.

Prior, D.J., Trimby, P.W., Weber, U.D., Dingley, D.J., 1996. Orientation contrast imaging of microstructures in rocks using forescatter detectors in the scanning electron microscope. Mineralogical Magazine 60, 859–869.

Reischmann, T., 1998. Pre-Alpine origin of tectonic units from the metamorphic core complex of Naxos, Greece, identified by single zircon Pb/Pb dating. Bulletin of the Geological Society of Greece 32, 101–111.

Riedl, H., 1982a. Vergleichende Untersuchungen zur Geomorphologie der Kykladen unter besonderer Berücksichtigung der Insel Naxos. Salzburger Exkursionsberichte 8, 9–54.

Riedl, H., 1982b. Die Altflächenentwicklung der Kykladen. Annales Geologiques des Payes Hélleniques 31, 33–84.

Ring, U., Glodny, J., Will, J., Thomson, S., 2010. The Hellenic subduction system: high-pressure metamorphism, exhumation, normal faulting, and large-scale extension. Annual Review of Earth and Planetary Sciences 38, 45–76.

Rösler, G., 1978. Relics of non-metamorphic sediments on central Aegean Islands. In: Closs, H., Roeder, D., Schmidt, K. (Eds.), Alps, Apennines, Hellenides. In: Stuttgart, E. (Ed.), Schweizerbart, Inter-union Commission on Geodynamics Scientific Report, 38, pp. 480–481.

Romeo, B., Capote, R., Lunar, R., 2007. Crystallographic preferred orientations and microstructure of a Variscan marble mylonite in the Ossa-Morena Zone (SW Iberia). Journal of Structural Geology 29, 1353–1368.

Rutter, E.H., 1998. On the relationship between the formation of shear zones and the form of the flow law for rocks undergoing dynamic recrystallization. Tectonophysics 303, 147–158.

Rutter, E.H., 1995. Experimental study of the influence of stress temperature and strain on the dynamic recrystallization of Carrara marble. Journal of Geophysical Research 100, 24,651–24,663.

Rutter, E.H., Casey, M., Burlini, L., 1994. Preferred crystallographic orientation development during the plastic and superplastic flow of calcite rocks. Journal of Structural Geology 16, 1431–1446.

Schenk, O., Urai, J., Evans, B., 2005. The effect of water on recrystallization behavior and grain boundary morphology in calcite-observations of natural marble mylonites. Journal of Structural Geology 27, 1856–1872.

Schenk, O., Urai, J.L., van der Zee, W., 2007. Evolution of boudins under progressively decreasing pore pressure – a case study of pegmatites enclosed in marble deforming at high grade metamorphic conditions, Naxos, Greece. American Journal of Science 307, 1009–1033.

Schmid, S.M., Casey, M., 1986. Complete fabric analysis of some commonly observed quartz C-axis patterns, in mineral and rock deformation: laboratory Studies. Geophysical Monograph Series 36, 263–286.

Schmid, S.M., Boland, J.N., Paterson, M.S., 1977. Superplastic flow in fine grained limestone. Tectonophysics 43, 257–291.

Schmid, S.M., Paterson, M.S., Boland, J.N., 1980. High temperature flow and dynamic recrystallization in Carrara marble. Tectonophysic 65, 245–280.

Seward, D., Vanderhaeghe, O., Siebenaller, L., Thomson, S., Hibsch, C., Zingg, A., Holzner, P., Ring, U., Duchêne, S., 2009. Cenozoic tectonic evolution of Naxos Island through a multi-faceted approach of fission-track analysis. In: Geological Society London, Special Publications, vol. 321, pp. 179–196. http://dx.doi.org/10.1144/SP321.9.

Siebenaller, L., Boiron, M.C., Vanderhaeghe, O., Hibsch, C., Jessell, M.W., Andremayer, A.S., France-Lanord, C., Photlades, A., 2013. Fluid record of rock exhumation across the brittle–ductile transition during formation of a Metamorphic Core Complex (Naxos Island, Cyclades, Greece). Journal of Metamorphic Geology 31, 313–338.

Stipp, M., Stünitz, H., Heilbronner, R., Schmid, S., 2002. The eastern Tonale fault zone: a 'natural laboratory' for crystal plastic deformation of quartz over a temperature range from 250 to 700 °C. Journal of Structural Geology 24, 1861–1884.

Stipp, M., Tullis, J., 2003. The recrystallized grain size piezometer for quartz. Geophysical Research Letters 30, 2088. http://dx.doi.org/10.1029/2003GL018444.

Stipp, M., Tullis, J., Scherwath, M., Behrmann, J.H., 2010. A new perspective on paleopiezometry: dynamically recrystallized grain size distributions indicate mechanism changes. Geology 38, 759–762.

Strumpf, N., 1997. Das Kernkristallin von Naxos (Kykladen, Griechenland). Berlin. Schriftenreihe für Geowissenschaften 5, 1–140.

Toy, V.G., Prior, D.J., Norris, R.J., 2008. Quartz fabrics in the Alpine Fault mylonites: Influence of pre-existing preferred orientations on fabric development during progressive uplift. Journal of Structural Geology 30, 602–621.

Twiss, R.J., 1980. Static theory of size variations with stress for subgrains and dynamically recrystallized grains, in U.S.G.S. Open-file Report 80-625, 665–683.

Twiss, R.T., 1977. Theory and applicability of a recrystallized grain size paleopiezometer. Pure and Applied Geophysics 115, 227–244. http://dx.doi.org/10.1007/BF01637105.

Urai, J.L., Schuiling, R.D., Jansen, J.B.H., 1990. Alpine deformation on Naxos (Greece). In: Geological Society London, Special Publication, vol. 54, pp. 509–522.

Urai, J.L., Feenstra, A., 2001. Weakening associated with the diaspore-corundum dehydration reaction in metabauxites; an example from Naxos (Greece). Journal of Structural Geology 23, 941–950.

Vanderhaeghe, O., 2004. Structural development of the Naxos migmatite dome. In: Whitney, D.L., Teyssier, C., Siddoway, C.S. (Eds.), Gneiss Domes in Orogeny, Geological Society of America Special Paper, 380, pp. 211–227.

Vanderhaeghe, O., Hibsch, C., Siebenaller, L., Duchêne, S., de St Blanquat, M., Kruckenberg, S., Fotiadis, A., Martin, L., 2007. Penrose conference – extending a continent – naxos field guide. In: Lister, G., Forster, M., Ring, U. (Eds.), Inside the Aegean Metamorphic Core Complexes. Journal of the Virtual Explorer vol. 27. http://dx.doi.org/10.3809/jvirtex.2007.00175.

Walcott, C., White, S., 1998. Constraints on the kinematics of post-orogenic extension imposed by stretching lineations in the Aegean region. Tectonophysics 298, 155–175.

Walker, A.N., Rutter, E.H., Brodie, K.H., 1990. Experimental study of grain-size sensitive flow of synthetic, hot-pressed calcite rocks. Geological Society Special Publications 54, 259–284.

Warren, J.M., Hirth, G., 2006. Grain size sensitive deformation mechanisms in naturally deformed peridotites. Earth and Planetary Science Letters 248, 438–450. http://dx.doi.org/10.1016/j.epsl.2006.06.006.

Wawrzenitz, N., Krohe, 1998. Exhumation and doming of the Thasos metamorphic core complex (S Rhodope, Greece). Structural and geochronological constraints. Tectonophysics 285, 301–332.

Wenk, H.R., Takeshita, T., Bechler, E., Erskine, B.G., Matthies, S., 1987. Pure shear and simple shear calcite textures. Comparison of experimental, theoretical and natural data. Journal of Structural Geology 9, 731–745.

Wernicke, B., 1985. Uniform sense simple shear of the continental lithosphere. Canadian Journal of Earth Sciences 22, 108–125.

Wernicke, B., Axen, G.J., 1988. On the role of isostasy in the evolution of normal fault systems. Geology 16, 848–851.

Whitney, D.L., Teyssier, C., Rey, P., Buck, R.W., 2013. Continental and oceanic core complexes. Geological Society of America Bulletin 125, 273–298.

Wijbrans, J.R., McDougall, I., 1986. $^{40}Ar/^{39}Ar$ dating of white micas from an Alpine high-pressure metamorphic belt on Naxos Greece): the resetting of the argon isotopic system. Contributions to Mineralogy and Petrology 93, 187–194.

Wijbrans, J.R., McDougall, I., 1988. Metamorphic evolution of the Attic Cycladic metamorphic belt on Naxos (Cyclades, Greece) utilizing $^{40}Ar/^{39}Ar$ age spectrum measurements. Journal of Meramorphic Geology 6, 571–594. http://dx.doi.org/10.1111/j.1525-1314.1988.tb00441.x.

Wortel, M.J.R., Spakman, W., 2000. Subduction and slab detachment in the Mediterranean–Carpathian region. Science 290, 1910–1917.